CHAPTER 8

Morphology of Vesicles

U. SEIFERT

Institut für Festkörperforschung, Forschungszentrum Jülich, 52425 Jülich, Germany

R. LIPOWSKY

Max-Plank-Institut für Kolloid- und Grenzflächenforschung, Kantstr. 55, 14153 Teltow-Seehof, Germany

Handbook of Biological Physics
Volume 1, edited by R. Lipowsky and E. Sackmann

Contents

1. Introduction: the shapes of vesicles

All biological cells contain complex mixtures of macromolecules not present in their environment. The 'container' of these cells is provided by the plasma membrane. This membrane forms a closed bag which is essentially impermeable for the macromolecules. Likewise, many organelles or compartments within the cells are surrounded by additional membranes which ensure that different compartments can have a different composition of molecules. The biomembranes of all present-day cells are composed of lipids and amphiphilic proteins. In fact, the basic and universal building block of all biomembranes seems to be a lipid bilayer which is 'decorated' by proteins.

Biomembranes exhibit a rather complex morphology [1]. The surface formed by intracellular organelles often have a very complicated topology such as those of the endoplasmatic reticulum or the Golgi apparatus. Likewise, the plasma membrane can develop small buds as in exo- or endocytosis, microvilli, i.e. finger-like protrusions, and pseudopods. These dynamic shape transformations are used in cell locomotion.

Some aspects of these morphological transformations can be studied with lipid vesicles which are closed bags formed spontaneously from lipid bilayers in aqueous solutions. These vesicles provide the simplest model system for the formation of distinct compartments in biological systems. They can conveniently be studied with video microscopy.

The current theoretical understanding of the morphology and morphology transformations of vesicles is based on the important notion of bending elasticity introduced some twenty years ago by Canham [2], Helfrich [3, 4] and Evans [5]. However, a systematic analysis of these so-called curvature models was performed only recently [6–9]. These studies revealed a large variety of shapes which minimize the energy for certain physical parameters such as the enclosed volume and the area of the vesicle. These shapes are then organized in so-called 'phase diagrams' in which trajectories predict how the shape transforms as, e.g., the temperature is varied.

As an example for this approach, see fig. 1, where the most prominent shape transformation, the budding transition, is shown as it has been observed by video microscopy [7, 10, 11]. An increase in temperature transforms a quasi-spherical vesicle via thermal expansion of the bilayer to a prolate shape and then to a pear. Finally, a small bud is expelled from the vesicle. Upon further increase of temperature several additional buds can emerge. Usually, the buds remain connected to the mother vesicle via narrow constrictions or necks. Another shape transformation, the discocyte–stomatocyte transition, is shown in fig. 2. This transition resembles a shape transformation which can be induced with red-blood cells by depletion of cholesterol.

Fig. 1. Budding transition induced by temperature which is raised from 31.4 °C (left) to 35.8 °C (right) in this sequence. The theoretical shapes have been obtained within the bilayer-couple model assuming an asymmetric thermal expansion of the two monolayers [7].

Fig. 2. Discocyte-Stomatocyte transition induced by temperature which is raised from 43.8 °C (left) to 44.1°C (right) in this sequence [7].

Shape transformations are also predicted to arise in vesicles consisting of a bilayer with several components due to a different mechanisms. If the two components form domains, the line energy associated with these domain boundaries can be reduced by budding of such a domain [12]. Even if the membrane is in the one-phase region, a temperature induced budding process should lead to curvature-induced phase segregation since, in general, the two components couple differently

to the local curvature [13]. So far, these effects are not yet verified experimentally even though budding and fission have been observed in vesicles consisting of lipid mixtures [14].

Qualitative new behavior has been predicted for vesicles with non-spherical topology, i.e. vesicles with holes or handles. For tori, i.e. vesicles with one hole or handle, the shape of lowest energy is non-axisymmetric for a large range of parameters [15, 16]. For shapes with at least two holes or handles, one even predicts that the shape of lowest energy is no longer unique. This degeneracy leads to the phenomenon of 'conformal diffusion' in shape space [17]. The simplest examples of artificial vesicles with non-trivial topology are shown in fig. 3 [18, 19].

The interaction of vesicles with substrates (or other vesicles) also effects their shape. For weak adhesion, an adhesion transition driven by the competion between bending elasticity and adhesion energy is predicted [20, 21]. For strong adhesion, the notion of an effective contact angle becomes applicable [20]. Experimentally, the adhesion of vesicles can be studied either with the micro-pipet aspiration technique [22] or by reflection interference microscopy [23, 24]. The latter technique allows very precise length measurements and, thus, to deduce the shape of adhering vesicles. In this way, a flat pancake can be distinguished from a quasi-spherical shape which is only slightly distorted by the adhesion to the substrate.

In this chapter, we describe the present understanding of these phenomena with an emphasis on the theoretical aspects. However, we make an attempt to link the theory with the experiments where this is possible. Various aspects of the work presented here have also been treated in recent reviews, see refs [25–27].

2. Bending elasticity and curvature models

2.1. Physical guidelines

In equilibrium, we can neglect processes such as hydrodynamic flows, convection or transport related to temperature gradients. Vesicles will then acquire the shape at which their total energy is minimal. The modelling of such an energy is guided by the following essential features of lipid bilayers:

(i) Length-scale separation: The thickness of the bilayer is in the nanometer-range, while the typical size of the vesicles considered here is in the micrometer-range, i.e. three orders of magnitudes larger.

(ii) Fluidity: The membrane is taken to be in its fluid state. Thus, it does not resist shear forces within the plane of the membrane.

(iii) Insolubility: Lipid molecules are practically insoluble in the aqueous medium, i.e. the number of molecules in the membrane remains essentially constant on experimentally relevant time-scales.

(iv) Bilayer architecture: The membrane is a bilayer consisting of two monolayers which do not exchange lipid molecules on the time-scale where the shape transformations take place. In addition, the monolayers can freely glide over one another, being coupled only through a constant separation and the topological constraint of forming a closed surface. These characteristics are less

Fig. 3. Vesicles of non-spherical topology. (a) a non-axisymmetric torus, (b) an axisymmetric torus, and (c) a 'button' shape [18, 19].

universal than those mentioned above. For instance, cholesterol is known to flip between the two monolayers on shorter time-scales [28]. Likewise, interdigitated states (which, so far, have not been found in fluid phases) do not exhibit this bilayer architecture.

2.2. Derivation of spontaneous-curvature model

The length-scale separation allows the vesicle to be described as a closed two-dimensional surface $\mathbf{R}(s_1, s_2)$ embedded in three-dimensional space. Here, s_1 and s_2

denote (arbitrary) internal coordinates. Such a surface can be locally characterized by its two radii of curvature R_1 and R_2 which determine the mean curvature H and the Gaussian curvature K, see fig. 4. These important quantities are defined as

$$H \equiv (1/R_1 + 1/R_2)/2, \tag{1}$$

and

$$K \equiv 1/(R_1 R_2). \tag{2}$$

Note that the radii R_1 and R_2 carry a sign. In particular, saddle surfaces can have vanishing mean curvature if the absolute value of the two radii of curvature are the same. Surfaces with $H = 0$ everywhere are called minimal surfaces.

The curvature model for vesicles is based on the assumption that the local energy, f_1, associated with bending the membrane can be expanded in H and K. For small deformations, the most general expression symmetric in R_1 and R_2 up to second order in $1/R_{\mathrm{i}}$ can be written as [3]

$$f_1 \equiv (\kappa/2)(2H - C_0)^2 + \kappa_{\mathrm{G}} K. \tag{3}$$

This expression contains three material parameters. The parameter κ is the bending rigidity. Typical values for phospholipid bilayers are of the order of 10^{-19} J, see section 2.6. The Gaussian bending rigidity, κ_{G}, is difficult to measure for reasons discussed below. However, κ_{G} and κ are expected to be of the same order of magnitude. Stability with respect to the spontaneous formation of saddles would require $\kappa_{\mathrm{G}} < 0$. A somewhat different expression for the local bending energy based on the combination $|1/R_1 - 1/R_2|$ has recently been discussed in ref. [29].

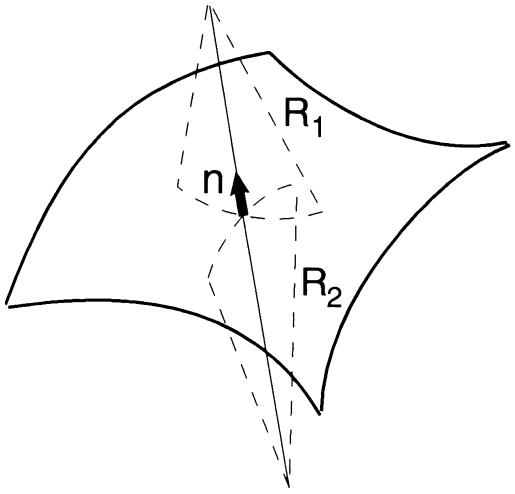

Fig. 4. Curvature on a two-dimensional surface. The length scales R_1 and R_2 denote the radii of curvature. The vector **n** denotes the normal.

The spontaneous curvature C_0 reflects a possible asymmetry of the membrane, justified either by a different chemical environment on both sides of the membrane or by a different composition of the two monolayers. (Note, however, that we have not yet incorporated the bilayer architecture and therefore the latter justification seems somewhat premature at this stage.) C_0 is usually assumed to be laterally homogeneous; this implies that it does not depend on the local shape of the membrane. So far, no direct measurements of C_0 are available for phospholipid vesicles.

The local energy (3) does not contain any quantity characterizing the internal degrees of freedom in the membrane. As a first step, it will be useful to include at least one additional variable which is suggested by the fluidity of the membrane. A fluid can be characterized by its local density $\phi(s_1, s_2)$. Small deviations of this density from the equilibrium density ϕ_0 lead to an elastic energy

$$f_2 = k(\phi/\phi_0 - 1)^2, \tag{4}$$

with an elastic compression modulus k.

Adding these two energies and integrating them over the closed vesicle surface yields the total energy

$$F = (\kappa/2) \oint \mathrm{d}A\ (2H - C_0)^2 + \kappa_{\mathrm{G}} \oint \mathrm{d}A\ K + (k/2) \oint \mathrm{d}A\ (\phi/\phi_0 - 1)^2. \tag{5}$$

This energy depends on the shape as well as on the density distribution $\phi(s_1, s_2)$. In this simplified model, the density distribution does not couple to the shape. Therefore, the last term in (5) is minimal for a uniform density. Because of the insolubility of the molecules, one can further minimize the energy F with respect to the total area, A, subject to the constraint $\oint \mathrm{d}A\phi = N$, where N is the total number of molecules in the membrane. This leads to

$$F = (\kappa/2) \oint \mathrm{d}A\ (2H - C_0)^2 + \kappa_{\mathrm{G}} \oint \mathrm{d}A\ K + (k/2)(A - A_0)^2/A_0, \tag{6}$$

where $A_0 \equiv N/\phi_0$ is the equilibrium area. Here and below, we have neglected higher order contributions in $(A - A_0)/A_0$. Since the bending rigidities κ and κ_{G} are of the order of 10^{-12} J, while $k \simeq 10^2$ mJ/m^2, see section 2.6, curvature energies can balance only minute deviations of the area A from its equilibrium value A_0. As a crude estimate, one obtains from balancing the first with the last term in (6) at constant enclosed volume that

$$|A - A_0|/A_0 \simeq (\partial F/\partial A)/k \simeq \kappa/kR_0^2 \simeq 10^{-8}$$

for $R_0 = 10\ \mu$m. Therefore, one ignores the elastic term and rather imposes the constraint of fixed total area.

A similar reasoning applies to the enclosed volume. Since the membrane is permeable to water, one might expect that the volume of the enclosed fluid can adjust freely. However, if additional molecules are present in the aqueous solution such as

ions or impurities, which cannot move through the membrane, any net transfer of water will lead to an osmotic pressure. Typically, such a pressure is huge on the scale of the bending energy. Consequently, the enclosed volume is essentially fixed by the number of enclosed, osmotically active molecules and by the concentration of these molecules in the exterior fluid through the requirement that the osmotic pressure is essentially zero [3].

In summary, the three properties (i) length-scale separation, (ii) fluidity and (iii) insolubility lead to the curvature energy

$$F_{\mathrm{SC}} = (\kappa/2) \oint \mathrm{d}A(2H - C_0)^2 + \kappa_{\mathrm{G}} \oint \mathrm{d}AK, \tag{7}$$

which has to be minimized at constant total area A and constant enclosed volume V. This constitutes the *spontaneous-curvature model* as introduced by Helfrich in 1973 [3].

Three mathematical properties of this energy should be noted. First, by virtue of the Gauss–Bonnet theorem the integral over the Gaussian curvature K is a topological invariant given by $4\pi(1 - g)$ where g is the genus, i.e the number of holes or handles, of the vesicles. As long as the topology does not change, the second term in eq. (7) can thus be ignored. Secondly, for $C_0 = 0$, the curvature energy is scale-invariant, i.e. the energy of a vesicle does not depend on its size since $\oint \mathrm{d}A\ H^2$ is a dimensionless quantity. Finally, the latter quantity is even invariant under general conformal transformations, see section 5.1.

2.3. Bilayer architecture and area-difference-elasticity model

So far, no explicit consideration has been given to the bilayer architecture. The relevance of the bilayer structure becomes evident through the following gedanken-experiment. Suppose an initially flat symmetric bilayer membrane is suddenly bent. This necessarily leads to a stretching of the outer monolayer and a compression of the inner one. The elastic energy stored in such a deformation can relax if the two monolayers glide over each other thus accommodating the local densities within each monolayer to the local shape [5, 30]. For a closed topology, however, this density relaxation can usually not succeed completely. As derived in the Appendix, there remains a contribution to the energy whenever the number of molecules within the two monolayers does not fit with the shape. This energy can be written as an area-difference-elasticity

$$F_{\mathrm{ADE}} \equiv \frac{\bar{\kappa}\pi}{8A_0 d^2} (\Delta A - \Delta A_0)^2, \tag{8}$$

since it attributes an elastic energy to deviations of the area difference, ΔA, between the two monolayers from the equilibrium value ΔA_0. Using a simple geometrical relation, ΔA is given by the total mean curvature M according to

$$\Delta A \approx 4d \oint \mathrm{d}AH \equiv 4dM \tag{9}$$

for a separation of $2d$ between the (neutral surfaces of the) two monolayers up to corrections of order dH and d^2K. The equilibrium value ΔA_0 is determined by the numbers N^+ and N^- of lipid molecules within each layer and by the equilibrium density ϕ_0 according to

$$\Delta A_0 = \left(N^+ - N^-\right)/\phi_0. \tag{10}$$

Since the non-local character of this energy arises from equilibration of the densities within each monolayer, the model implicitly assumes that the time-scale of the phenomena we are interested in is larger than the typical time-scale for this equilibration which takes place via propagating sound waves.

The full energy in the area-difference-elasticity model, W, then reads [31–33]

$$W \equiv (\kappa/2) \oint \mathrm{d}A(2H)^2 + \frac{\bar{\kappa}\pi}{8A_0 d^2} (\Delta A - \Delta A_0)^2. \tag{11}$$

It has been introduced in 1991 by three groups independently based on much earlier work by Evans [5, 34] and Sheets and Singer [35]. The first term in eq. (11) is the scale-invariant local bending energy which is broken by the area-difference elasticity if ΔA_0 is not rescaled properly.

The elastic constant $\bar{\kappa}$ in front of the second term is the so-called non-local bending rigidity. In the derivation given in the Appendix, it turns out to be

$$\bar{\kappa} \equiv \alpha\kappa \equiv 2k^{(m)}d^2/\pi. \tag{12}$$

If one assumes that the monolayers are homogeneous sheets of thickness $2d$, the monolayer rigidity $\kappa^{(m)} = \kappa/2$ is related to the monolayer compression modulus $k^{(m)}$ through

$$\kappa^{(m)} = k^{(m)}d^2/3. \tag{13}$$

This leads to the important estimate of $\alpha = \bar{\kappa}/\kappa = 3/\pi$. However, from a theoretical point of view it is convenient to leave the value of α open and to treat it as an independent material parameter. Moreover, the area-difference-elasticity model may be applicable even if a simple relation like (13) breaks down due to the internal structure of the monolayer. Likewise, the effective value of α for multilamellar vesicles can become larger since it is roughly quadratic in the number of bilayers [36] assuming a fixed inter-membrane separation.

For $\alpha = 0$, one recovers the spontaneous curvature model from the area-difference elasticity model, provided one replaces $2H$ by $2H - C_0$ in eq. (11). This applies to the case where the two monolayers are asymmetric in the first place which would leave an effective C_0 for the bilayer. The explicit derivation of the area-difference-elasticity model assuming monolayers with different C_0 requires some care in the definition of the neutral surfaces [37, 38, 39]. In fact, it turns out that the effect of a spontaneous curvature $C_0 \neq 0$ in the area-difference elasticity model is easy to determine theoretically since any $C_0 \neq 0$ can be mapped on a renormalization of the area-difference ΔA_0 [38, 39].

2.4. Bilayer-couple model

In the limit of large α, the elastic energy for the area-difference enforces the 'hard' constraint $\Delta A = \Delta A_0$. One thus recovers from the area-difference-elasticity model the so-called bilayer-couple model, introduced by Svetina and Zeks in 1983 based on the bilayer-couple hypothesis [40]. In view of the above derivation, the bilayer-couple model is based on the implicit assumption that the monolayers are incompressible.

2.5. Simple shapes of minimal energy

It is instructive to neglect initially the non-local energy contribution and to discuss simple shapes within the spontaneous curvature model ignoring the constraints on A and V. First, consider the shapes for which the local curvature energy, $(\kappa/2)\oint \mathrm{d}A\ (2H - C_0)^2$, vanishes. Obviously, spheres with radius $R = 1/C_0$ as well as cylinders with radius $R = 1/2C_0$ have zero curvature energy. In fact, a whole family of axisymmetric surfaces, the so-called unduloids, have $H = 1/2C_0$ and, therefore, zero curvature energy. These shapes interpolate between the cylinder and a necklace of spheres, see fig. 5. In particular, the narrow necks which the unduloid develops as it approaches the necklace conformation do not contain any curvature energy even though the absolute value of each radius of curvature becomes very small. Since these curvature radii have different signs, H retains a finite value. The evolution of these unduloids suggests that budding phenomena which are characterized by the occurrence of narrow necks might be understood within the framework of these curvature models.

The basic physical effect of the non-local energy contribution in (11) can be qualitatively understood as follows. A spherical vesicle with radius R_0 has an area

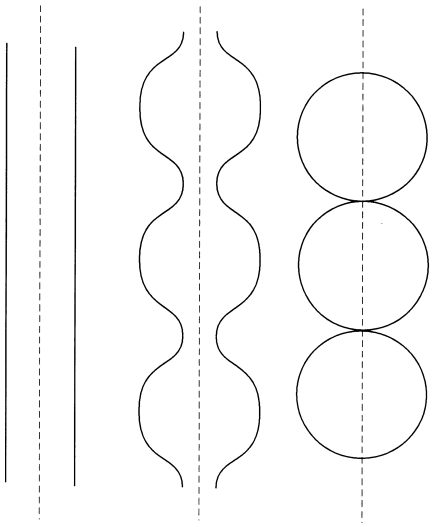

Fig. 5. Unduloids. All shapes are axisymmetric with respect to the broken line and have zero bending energy, since the mean curvature $2H = C_0 = \text{const}$ everywhere.

difference $\Delta A = 16\pi R_0 d$. If the equilibrium area difference ΔA_0 is larger, the non-local term will induce a driving force towards a shape which has a larger ΔA, i.e. a larger total mean curvature such as prolates or pear shapes. In fact, the limit shape of two spheres of equal radius $R_0/\sqrt{2}$ sitting on top of each other has an area difference of $\Delta A = \sqrt{2} \times 16\pi R_0 d$. Likewise, an equilibrium area difference which is smaller than the value of the sphere favors oblates, discocytes and stomatocytes (or invaginations).

2.6. Elastic material parameters

2.6.1. Bending rigidities

Great effort has been devoted in order to determine the bending rigidity κ. Conceptually, two different approaches can be distinguished. In the mechanical approach, the response of the membrane to an applied force is measured from which the bending rigidity is deduced. The extreme softness of these systems is exploited by the second type of methods where the bending rigidity is derived from the thermally excited membrane fluctuations.

One example for the mechanical approach [41, 42] is provided by studies of tether formation from giant vesicles which are aspirated with a micropipet [43]. The tether is pulled out by the gravitational force on a small glass bead which adheres to the vesicles surface. The length of the tether is determined by the balance of the suction pressure, the gravitational force and bending energies. It has been realized only recently, that, with this method, both the bending rigidity κ as well as the non-local bending rigidity, $\bar{\kappa} = \alpha\kappa$, can be measured simultaneously [44].

In the flickering experiments, the bending rigidity is derived from mean-square amplitudes of thermally excited membrane fluctuations using phase contrast microscopy combined with fast image processing. This technique has been used with quasi-spherical vesicles [45–50], shape fluctuations of tubular vesicles [51], fluctuations of almost planar membrane segments [52] and fluctuations of weakly bound vesicles [23, 53]. So far, all these experiments are analysed in terms of the local bending rigidity κ. The theoretical background for this method is given in section 4, where it is also pointed out that one can safely ignore the non-local contribution in the analysis of these experiments.

A third class of experiments combines the mechanical with the entropic approach. Since aspiration of the vesicle in the micropipet changes the area available for fluctuations [54], the strength of the fluctuation can be controlled mechanically. From the relation between the area stored in the fluctuations and the suction pressure which is related to the effective entropic tension, the bending rigidity can be deduced [55]. The same idea has also been used in a very different set-up where quasi-spherical vesicles are elongated in an AC electric field [56]. Again the bending rigidity is derived from the relation between the area stored in the fluctuations and the applied field which controls the tension.

The values obtained by these techniques are given in table 1 for different lipids. Even for the same lipid, the bending rigidity differs by a factor of 2 using different methods. Sometimes, the same technique applied by different research groups yields

Table 1
Experimental values for the bending rigidity κ.

Lipid	Temp. [°C]	κ [10^{-19}J]	Method	Ref.
DMPC		1.15 ± 0.15	Flickering of quasi-spherical vesicles	[49]
DMPC	26	0.35–0.65	Flickering of quasi-spherical vesicles	[46]
DMPC	29	0.56 ± 0.06	Entropic tension, micropipet	[55]
G–DG		0.15–0.4	Flickering of quasi-spherical vesicles	[49]
DGDG		0.12–0.27	Fluctuations of planar pieces	[52]
DGDG	23	0.44 ± 0.03	Entropic tension, micropipet	[55]
DGDG		$0.1 \pm 20\%$	Entropic tension, electric field	[56]
SOPC	18	0.9 ± 0.06	Entropic tension, micropipet	[55]
SOPC	18	2.0	Tether formation, micropipet	[43]
DAPC	18	0.44 ± 0.05	Entropic tension, micropipet	[55]
DMPC		1.0–2.0	Flickering of tubular vesicles	[51]
EYPC		0.4–0.5	Flickering of quasi-spherical vesicles	[48]
EYPC		1.15 ± 0.15	Flickering of quasi-spherical vesicles	[49]
EYPC		0.8	Fluctuations of planar pieces	[52]
EYPC		$0.25 \pm 20\%$	Entropic tension, electric field	[56]
DLPC		$0.34 \pm 20\%$	Entropic tension, electric field	[56]
POPC		$0.25 \pm 20\%$	Entropic tension, electric field	[56]
DMPC:DPPC 1:1		0.38–0.49	Flickering of quasi-spherical vesicles	[46]
DMPC + 20% CHOL		2.1 ± 0.25	Flickering of quasi-spherical vesicles	[49]
DMPC + 30% CHOL		4.0 ± 0.8	Flickering of quasi-spherical vesicles	[49]
SOPC:CHOL	15	2.46 ± 0.39	Entropic tension, micropipet	[55]

significantly different values. Whether these discrepancies have to be attributed to real physical effects such as impurities or to experimental problems needs further analysis. Likewise, the hypothesis put forward by Helfrich [57, 58] that these discrepancies support evidence for a superstructure of the membrane on suboptical scales still awaits direct verification, see chapter 14 in this book.

The bending rigidity for mixtures is particularly interesting given the fact that biological membranes always involve mixtures. Addition of cholesterol to fluid bilayers increases the bending rigidity (as well as the area compressibility) significantly [42, 49]. However, the non-local bending rigidity seems not to change with the addition of cholesterol [59]. This may be related to the fact that cholesterol can flip between the monolayers quite rapidly.

A significant decrease in the apparent bending rigidity of an order of magnitude follows from addition of a few (2–5) mol% of a short bipolar lipid (bola lipid) or small peptides (e.g., valinomycin) [49]. Since the apparent bending rigidity then becomes comparable to the thermal energy T, these vesicles exhibit very strong shape fluctuations. Entropic terms then become relevant for the description of typical conformations. One must note, however, that bola lipid is much more soluble in water and thus will go in and out of the bilayer more rapidly.

Table 2
Area compression modulus k and thermal expansion coefficient β of bilayers taken from ref. [42].

Lipid	k [mJ/m^2]	β [10^{-3}/K]
DMPC (29°)C	145 ± 10	6.8 ± 1.0
DMPC (35°)C		4.2 ± 0.2
SOPC (15°)C	200 ± 13	3.3 ± 0.7
SOPC:CHOL 1:1 (23°)C	1077 ± 167	1.62 ± 0.16
DMPC:CHOL 1:1 (22°)C	685	1.33

The Gaussian bending rigidity is difficult to measure experimentally since it is a topological invariant. In principle, it can be inferred from measurements on ensembles of vesicles which are equilibrated with respect to topological changes. To our knowledge, there is no experimental record of a topology change in single-component phospholipid bilayer vesicles. Thus, one can conclude that the time-scale for such changes is quite large. For vesicles containing several domains, on the other hand, the Gaussian bending rigidity should have observable effects even for a single vesicle [60].

2.6.2. Area compression modulus

The area compressibility k does not enter the curvature energy. However, many experiments involve stretching of the membrane which is governed by this quantity. Detailed values as determined by micro-pipet aspiration can be found in the review by Evans and Needham [42] from which a table is reprinted here as table 2. A typical order of magnitude is $k \simeq 10^2$ mJ/m^2. This value is indeed compatible with the order of magnitude of the bending rigidity, $\kappa = 10^{-19}$ J, since the relation $\kappa = kd^2/3$ from continuum mechanics for a thin homogeneous plate of thickness $2d$ then leads to $2d \simeq 3.5$ nm, which is a typical bilayer thickness.

2.6.3. Thermal expansion coefficient

The thermal area expansion coefficient β which enters the calculation of temperature trajectories can also be determined by micro-pipet aspiration. Values are also given in table 2 again taken from Evans and Needham [42].

3. Shapes of minimal energy and shape transformations

3.1. Theoretical methods

The first step towards a systematic theory based on curvature models is to calculate the shapes of lowest energy. Since for phospholipid membranes, the bending rigidity κ is large compared to the thermal energy T, thermal fluctuations around the shape of lowest energy can be ignored in such a first step. This holds for vesicles which are small compared to the persistence length $\xi_p \equiv a \exp(2\pi\kappa/T)$, where a is a molecular scale of the order of nanometers [61]. For phospholipid membranes, this length scale

is astronomical. If the size of the vesicle becomes comparable or larger than ξ_p, thermal fluctuations lead to irregular shapes which can theoretically be investigated by Monte Carlo simulation [62].

In general, one obtains different types (or families or branches) of shapes of lowest energy in different regions of the parameter space. This division of the parameter space represents the so-called phase diagram of the model.

So far, the complete phase diagram has not been obtained for any curvature model since, in most cases, the minimization of the corresponding curvature energy has only been performed within a certain subspace of shapes. A significant simplification arises if one restricts the problem to axisymmetric shapes. Whether this restriction which might look plausible is indeed permissible has to be checked *a posteriori*. The canonical procedure for the calculation of axisymmetric shapes of lowest energy is as follows [4, 6, 8, 9, 63–67]: First, the constraints of fixed volume and area are added to the curvature energy *via* Lagrange multipliers. Then, the axisymmetric shape is expressed in terms of its contour parameters. Stationarity of the shape leads to the Euler Lagrange equations corresponding to the curvature energy (augmented with the constraints). These coupled non-linear differential equations have to be solved numerically. The solutions (the so-called stationary shapes) can be organized in branches due to their symmetry properties. The most important branches are the prolate and oblate ellipsoids which include the dumbbells and discocytes, respectively. Pear-shaped vesicles and stomatocytes bifurcate from the prolate and the oblate branch, respectively. Since the solutions to the shape equations contain local energy minima as well as unstable saddle points one has to check the stability of each solution. Stability with respect to axisymmetric deformations follows from a close inspection of the bifurcation diagram [9]. Stability with respect to non-axisymmetric perturbations requires additional work which has not yet been performed in a systematic way [65, 68] except in the spherical limit [69–73]. However, stability under general conformal transformations has been studied systematically, see section 5.1 below.

All the curvature models introduced above, lead to the same set of stationary shapes since they only differ in global energy terms. However, the stability of these shapes and, thus, the phase diagram depends crucially on the specific model and the corresponding model parameters.

3.2. A simple model: Local curvature energy only

To illustrate the general procedure described above, consider the spontaneous curvature model for $C_0 = 0$ together with the constraints on the area A and the enclosed volume V [9]. Since the curvature energy is scale-invariant in this case, only the reduced volume

$$v \equiv V/\left[4\pi R_0^3/3\right] \tag{14}$$

enters, where

$$A \equiv 4\pi R_0^2 \tag{15}$$

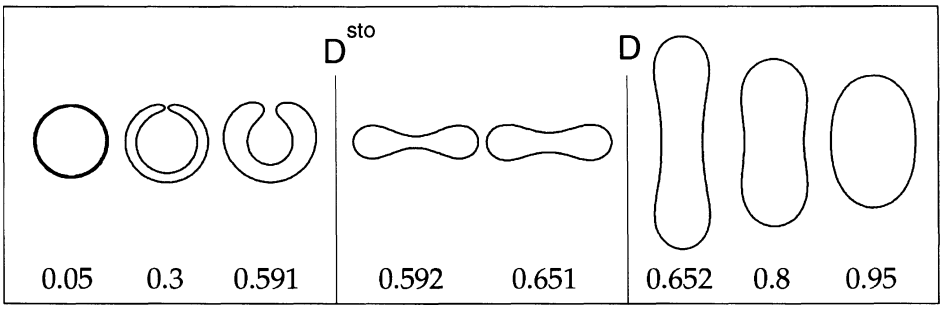

Fig. 6. Shapes of lowest bending energy for spontaneous curvature $C_0 = 0$ and several values of the reduced volume v. D and D^{sto} denote the discontinuous prolate/oblate and oblate/stomatocyte transition, respectively. All shapes have the same area [9].

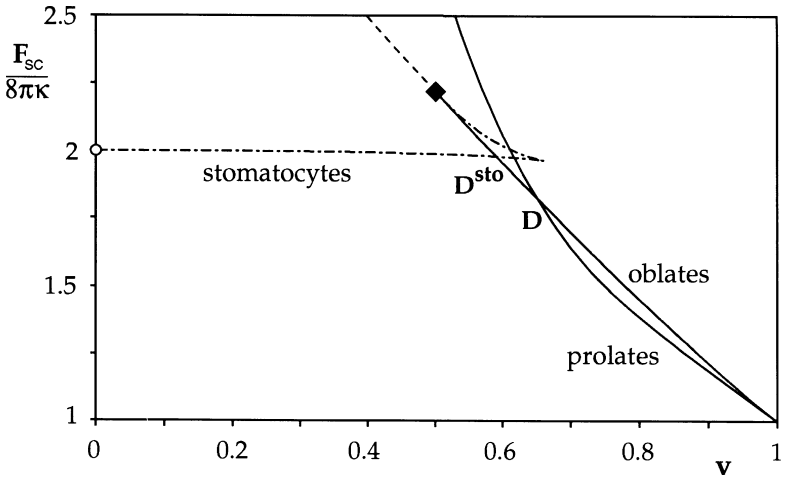

Fig. 7. Bending energy F_{SC} as given by (7) for $C_0 = 0$ (and $\kappa_{\mathrm{G}} = 0$) as a function of the reduced volume v. Three branches of stationary shapes are displayed: the prolate, the oblate and the stomatocyte branch. The latter bifurcates from the oblate branch. Its upper part between the bifurcation and the cusp corresponds to locally unstable shapes. Its lower part correspond to locally stable shapes. The oblate branch beyond the diamond corresponds to selfintersecting (and thus unphysical) states [9].

defines the equivalent sphere radius R_0. Such a model is presumably the simplest model for a vesicle consisting of a symmetric bilayer. It should be applicable to membranes with fast flip-flop between the two monolayers.

For $v = 1$, the shape is necessarily a sphere, while for $v < 1$, the solutions to the shape equations are prolate ellipsoids and dumbbells, oblate ellipsoids and discocytes, and stomatocytes. Typical shapes as well as their energy are shown in figs 6 and 7 taken from ref. [9]. For $v \lesssim 1$ the prolates have lowest energy. For $v < 0.65$, the energy of the oblates becomes smaller than the energy of the prolates. This amounts to a discontinuous transition from the prolates to the oblates with decreasing v. For any discontinuous transition, it is important to know for which value of the reduced

volume a metastable shape looses its local stability. Approaching the transition from either the small or the large v-values, the shapes will be trapped in the local (metastable) minimum as long as the thermal energy is not sufficient to overcome the barrier for the transition towards the global minimum. An approximate stability analysis shows that the prolates are locally stable for all v whereas the oblates loose local stability with increasing v at some value v_* with $0.7 < v_* < 0.85$ [73]. Thus, for large reduced volume, the oblates whose energy is shown in fig. 6 correspond to saddle points.

The energy diagram shown in fig. 7 directly reveals, that for even smaller volume, the oblates become unstable with respect to an up/down symmetry breaking for $v < 0.51$. This type of instability which preserves the axisymmetry can be read off from the bifurcation diagram. It is then also obvious that the upper part of the stomatocyte branch corresponds to the saddle point between a locally stable oblate and a locally stable stomatocyte. This energy diagram leads to a discontinuous transition between the oblate and the stomatocytes at $v \simeq 0.59$. The limits of metastability are at $v \simeq 0.66$ for the stomatocyte and $v \simeq 0.51$ for the oblate, respectively.

Two facts about this simple model should be emphasized: (i) The biconcave discocytes have lowest energy in a narrow range of reduced volume v. Thus a negative C_0 is not required to obtain these red-blood-cell like shapes contrary to repeated claims in the older literature. (ii) Budding does not occur in this model since pears do not show up as stationary shapes for vanishing spontaneous curvature.

3.3. Phase diagrams

3.3.1. Spontaneous-curvature model

The phase diagram in the spontaneous-curvature model is shown in fig. 8 taken from [9]. Apart from the reduced volume v, it depends on the scaled spontaneous curvature

$$c_0 \equiv C_0 R_0. \tag{16}$$

It contains large regions of stomatocytes, oblates/discocytes, prolates/dumbbells and pear-shaped vesicles. A negative C_0 favors stomatocytes while a positive C_0 leads to pear-shaped vesicles which are involved in the budding transition [8, 9, 66, 74, 75]. In particular, the pear shapes end up at a curve L^{pear} along which the neck diameter of the pears tends to zero. The shapes then consist of two spheres with radii R_1 and R_2 which are connected by a narrow neck. For such an 'ideal' neck, one has the 'kissing condition' [8, 9, 66, 75]

$$1/R_{\text{A}} + 1/R_{\text{B}} = C_0. \tag{17}$$

Here, R_{A} and R_{B} denote the local radii of curvatures of the two adjacent segments extrapolated through the neck which are necessarily equal at the poles in each individual segment. This kissing condition can be phenomenologically derived by the requirement that the energy density $(2H - C_0)^2$ is the same for the two adjacent

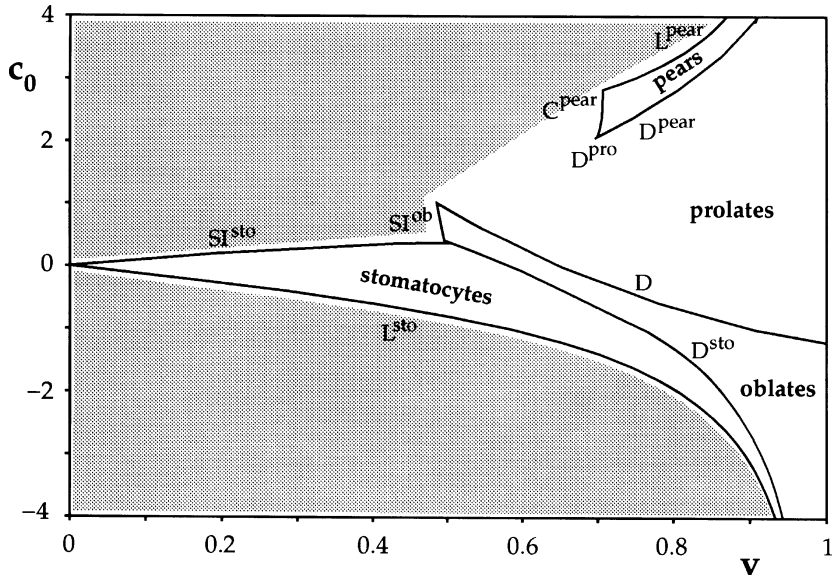

Fig. 8. Phase diagram of the spontaneous-curvature model. This phase diagram shows the shape of lowest bending energy as a function of the scaled spontaneous curvature c_0 and of the reduced volume v. The regions where the prolate/dumbbell, pear-shaped, oblate/discocyte and stomatocytes have lowest energy are separated by transition lines. The line C^{pear}denotes a continuous transition. All other transitions are discontinuous. The lines L^{sto} and L^{pear} correspond to limit shapes with infinitesimal neck. Beyond the lines $SI^{ob}$and SI^{sto} selfintersecting states occur. In the shaded area, the shape of lowest energy has still to be determined [9].

segments. As a thorough mathematical analysis shows it also holds for more complicated budding processes where spheres and prolates are connected by this type of neck [76]. Beyond the limiting line L^{pear}, the phase diagram becomes quite complicated since further branches of shapes appear which involve a prolate connected to a sphere or shapes of multiple segments [8]. In this region, additional energy terms such as attractive Van der Waals interaction can become relevant [77, 78].

Two general features of the phase diagram of the spontaneous-curvature model should be kept in mind: (i) Most transitions are discontinuous, i.e. one expects large hysteresis effects. (ii) Even though one cannot exclude the possibility that somewhere in the phase diagram the ground-state of the vesicle is non-axisymmetric, there are so far no indications for such a region.

3.3.2. Bilayer-couple model

In the bilayer-couple model, the phase diagram depends on the reduced area difference

$$\Delta a \equiv \Delta A/16\pi R_0 d \tag{18}$$

and the reduced volume v. The phase diagram [9] is shown in fig. 9. Qualitatively speaking, ΔA takes over the role of the spontaneous curvature. A large ΔA promotes

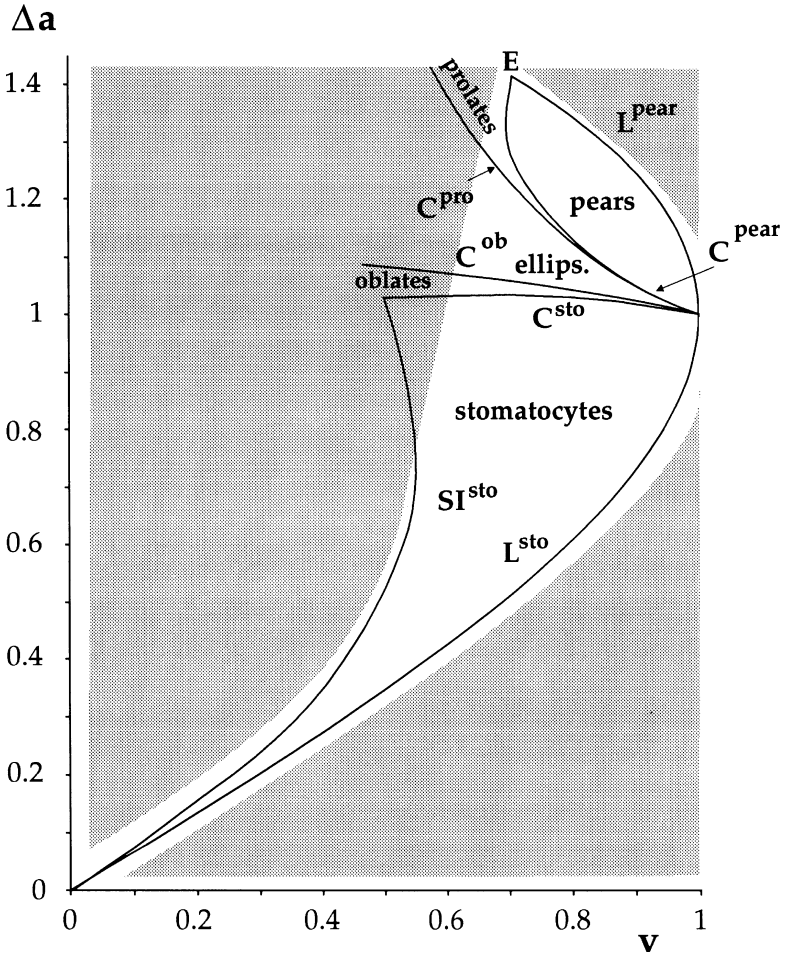

Fig. 9. Phase diagram of the bilayer-couple model. This phase diagram shows the state of lowest energy as function of the reduced area difference Δa and of the reduced volume v. C^{pear} denotes the line of continuous transitions between up-down symmetric prolate/dumbbell shapes and up-down asymmetric pear-shapes. Likewise, C^{sto} denotes the locus of the continuous transitions between the oblate/discocyte shapes and the stomatocytes. L^{pear} and L^{sto} are limit curves which correspond to budding and the inclusion of a spherical cavity, respectively. In the region between the prolate/dumbbell and discocyte regime, non-axisymmetric ellipsoids have lowest energy. This region is separated by continuous transitions C^{pro} and C^{ob} from the corresponding axisymmetric shapes. E denotes the point where two spheres of equal radii are sitting on top of each other. Along the line SI^{sto}, the two poles of the shape touch each other. In the shaded areas, the shape of lowest energy has not been determined so far [9].

pear-shaped vesicles, while smaller values can lead to stomatocytes. However, two important differences to the phase diagram of the spontaneous-curvature model arise: (i) All transitions found so far are continuous, i.e. there are no metastable states and there are no hysteresis effects. (ii) A region of non-axisymmetric ellipsoids emerges

between the oblate and the prolate phases [9, 68, 73].

3.3.3. Area-difference-elasticity model

Since the area-difference-elasticity model interpolates between the spontaneous-curvature model and the bilayer-couple model, its phase diagram also interpolates between the two phase diagrams shown above. In fact, the phase diagram of the area-difference-elasticity model depends on three variables: the reduced volume v, the reduced equilibrium area-difference

$$\Delta a_0 \equiv \Delta A_0 / 16\pi R_0 d \tag{19}$$

and the parameter $\alpha = \bar{\kappa}/\kappa$ as discussed in section 2.3. Since the phase diagrams of the two limiting cases are notably different, one can expect that the full three-dimensional phase diagram reveals a complex topology. So far, mainly two parts of this three-dimensional phase diagram have been investigated in some detail, namely the oblate/prolate transition [68] and the budding region [31, 38, 39]. Rather than presenting the three-dimensional phase diagram here, we will discuss the specific part of the phase diagram which describes the budding region in relation to experimental results. To this end, we first need to know the effect of a temperature change on those variables which determine the shape.

3.4. Temperature trajectories

For a physical interpretation of the phase diagrams one has to relate the variables v, c_0, m_0 to physical observables which poses practical as well as fundamental problems. For an axisymmetric vesicle, the area and the volume can be inferred, in principle, from its contour, if the orientation of the symmetry axis is known. However, thermal fluctuations as well as rotational diffusion of the vesicle limit the resolution. No direct measurements of the total mean curvature M which would yield ΔA, compare eq. (9), have been performed so far even though this quantity could also be obtained from the contour through higher derivatives.

As for the spontaneous curvature C_0 and the equilibrium area-difference ΔA_0, the situation is different since these quantities cannot be measured directly. Even though a certain amount of theory exists on the effective spontaneous curvature induced by different electrostatic parameters on the two sides of the bilayer (compare chapter 12 in this volume), there is no practical method for determining the spontaneous curvature directly for phospholipid bilayer vesicles. In a symmetric environment, however, one would expect that $C_0 = 0$. Likewise, the equilibrium area-difference ΔA_0 is not accessible to any direct measurement, compare section 3.6 below. According to (10), ΔA_0 depends on the number of molecules in the two monolayers which is determined by the preparation process.

Given this somewhat unsatisfying situation, one has to be content with a knowledge of the relative variation of these parameters upon changing a physical control parameter. The most widely used parameter, so far, is the temperature T which can be controlled within 0.1°C. An increase in temperature from an initial value T_0 leads to a thermal expansion of the area of the two monolayers. It will be necessary to

consider a small asymmetry γ of the expansion coefficients of the two monolayers [7, 9], β^{in} and β^{ex}, defined as

$$\beta^{\text{in}} \equiv \frac{1}{A^{\text{in}}}\,\frac{\partial A^{\text{in}}}{\partial T} \equiv \beta \quad \text{and} \quad \beta^{\text{ex}} \equiv \frac{1}{A^{\text{ex}}}\,\frac{\partial A^{\text{ex}}}{\partial T} \equiv (1+\gamma)\beta. \tag{20}$$

A typical value is $\beta \simeq 6 \times 10^{-3}/K$ which is one order of magnitude larger than the expansion coefficient for the enclosed aqueous solution. The latter can therefore be neglected. However, one has to take into account that the thickness $2d$ of the bilayer also becomes temperature dependent according to

$$\frac{1}{d}\,\frac{\partial d}{\partial T} \equiv \beta_d. \tag{21}$$

Assuming temperature independent expansion coefficients, one finds for a temperature trajectory the expression

$$\Delta a_0 = \big(v(T_0)/v\big)^r \big\{\Delta a_0(T_0) + b\big[\big(v(T_0)/v\big)^{\gamma q} - 1\big]\big\}, \tag{22}$$

parametrized by an initial point with $\Delta a_0 = \Delta a_0(T_0)$ and $v = v(T_0)$ on the trajectory [7, 9]. The exponents are given by

$$q = (2+\gamma)/3, \tag{23}$$

and

$$r = \frac{2 - \gamma - 4\beta_d/\beta}{3(2+\gamma)}. \tag{24}$$

The latter value can be bounded theoretically by two limiting cases. (i) If the monolayer separation $2d$ does not change with temperature, one has $\beta_{\text{d}} = 0$ which leads to $r = 1/3$. (ii) If d decreases with temperature in such a way that the bilayer volume as given by $\sim Ad$ remains temperature independent, i.e. $\beta_{\text{d}} = -\beta$, one has $r = 1$. Experiments using nuclear magnetic resonance indicate that the latter case is a good approximation [79]. Without asymmetry, i.e. for $\gamma = 0$, one obtains the simple expression

$$\Delta a = \Delta a_0(T_0)\big(v(T_0)/v\big)^r. \tag{25}$$

However, even a small asymmetry γ of the order 10^{-3} has a considerable influence on the temperature trajectory [7] since the dimensionless coefficient b in (22) is given by

$$b \equiv A^{\text{ex}}(T_0)/\big\{8d(T_0)\big[\pi A(T_0)\big]^{1/2}\big\}. \tag{26}$$

It is proportional to the radius R_0 of the vesicle and becomes of the order of 10^3 for $R_0 \simeq 10$ μm. The physical basis for this tremendous effect is the length-scale separation emphasized in section 2. The relevant quantity for a change in shape is not only the absolute change in area, which mainly affects v, but also the variation of the area-difference in the two monolayers for which the relevant scale is of the order of dR_0. If the outer monolayer expands more than the inner one, the additional area accumulated in this outer layer will cause budding since the formation of buds increases the area difference. Likewise, a stronger increase of the area of the inner monolayer induces a transition to the discocytes and the stomatocytes.

This sensitive dependence of the thermal trajectory in the phase diagram indicates that it will be rather difficult in general to reproduce experiments on vesicle shape transformations. Presently, the available purity of the lipids does not exclude the presence of residual impurities which could result in an asymmetric expansion of the order of 10^{-3}. It would be highly beneficial to investigate this effect systematically by deliberately adding traces of a second (miscible) component to one of the monolayers. However, one then has to be aware of additional effects arising from the mixture, see section 6.

3.5. Temperature-induced budding

The discussion in the last section has demonstrated that even though temperature trajectories can be calculated in principle, direct comparison with experimental trajectories is difficult because not all of the relevant parameters are known. Therefore, it is reasonable to focus first on those qualitative aspects which can be treated even without detailed knowledge of the precise temperature trajectory.

As an example for such an approach, consider the phase diagram of the budding region in the area-difference elasticity model shown in fig. 10. This is a section of the three-dimensional phase diagram in the region where budding occurs at a fixed value of $\alpha = 4$, chosen here for illustrative purposes [39]. Two different cases for the budding transition can be distinguished: (i) For a relatively small reduced volume v, the symmetry-breaking budding transition between the prolates and the pear-shaped vesicles is continuous. Weak pears are therefore stable and an increase in Δa_0 will progressively increase the neck diameter until at L^{pear} the limit line, or vesiculation line, is reached. Along this line, the neck diameter has formally shrunk to zero. The shape then consists of two spheres sitting on top of each other. (ii) For a large reduced volume, the budding transition becomes discontinuous, with the line of instability extending well into the vesiculated region beyond the limiting line L^{pear}. Therefore, the theory for this value of α predicts a qualititative difference between budding at a small reduced volume and budding at a larger reduced volume.

At present the best estimate for α is $\alpha \simeq 1$, which is supported by derivations using standard elasticity theory as sketched in section 2.3 as well as by experimental measurements [44]. For such a value, the area-difference-elasticity model predicts a discontinuous budding transition irrespective of the reduced volume (if budding takes place at all).

These theoretical predictions are presently still in partial conflict with the experimental results. Experimentally, two apparently different scenarii for the budding

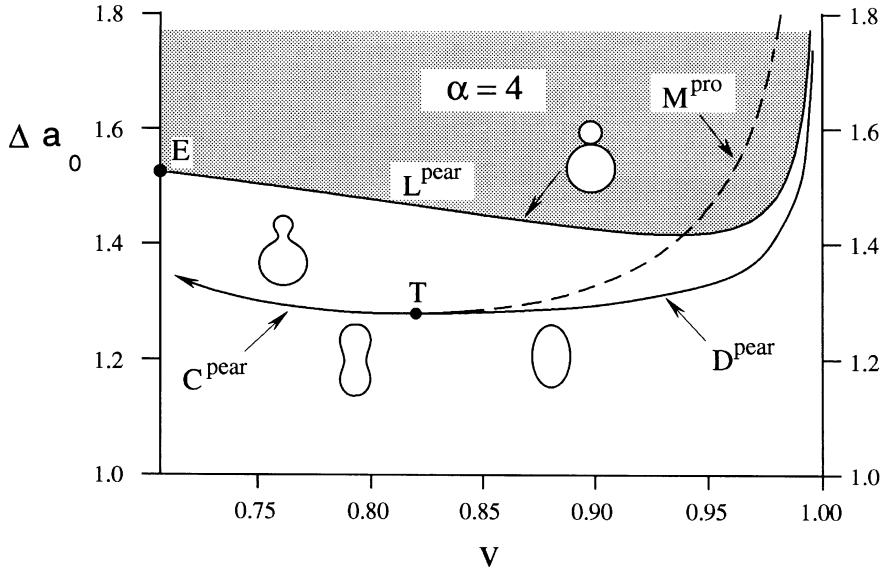

Fig. 10. Phase diagram of the area-difference-elasticity model in the budding region for rigidity ratio $\bar{\kappa}/\kappa = \alpha = 4$ as a function of the equilibrium area-difference Δa_0 and of the reduced volume v. The lines $C^{\text{pear}}$and D^{pear}denote a continuous and a discontinuous budding transition, respectively, separated by the tricritical point T. For a discontinuous transition, the prolates become infinitesimally unstable at the line M^{pro}. $L^{\text{pear}}$is the vesiculation curve where two spheres of different radii are connected by an ideal neck. At E, the two spheres have equal size [39].

transition can be distinguished: (i) For DMPC-vesicles, a slow increase in temperature leads continuously to a pear with weak up-down asymmetry which upon further temperature change jumps to a vesiculated shape with a narrow neck [7, 11]. (ii) For SOPC-vesicles in sucrose/glucose solutions, discontinuous budding is observed without the pear-shaped intermediates [80]. A similar sequence can also be obtained for DMPC-vesicles provided they are kept under some tension before the heating starts [11].

The second experimental scenario (ii) is compatible with the predictions of a discontinuous budding of the area-difference elasticity model for $\alpha \simeq 1$. To explain experimental scenario (i) within the area-difference elasticity model seems to be impossible. The apparent continuous transition from the symmetric shape to the pear with weak up-down asymmetry could be caused by a large α value, which is expected to apply for multilamellar vesicles if the bilayer are strongly coupled. However, the apparent transition from a wide neck to a narrow neck is not contained in any of the curvature models discussed so far. Therefore, even on this qualitative level, there remains a serious discrepancy between theory and experiment. Further energy terms beyond those contained in the area-difference-elasticity model could, in principle, provide such a scenario [78]. However, one expects any corrections to (11) arising from elastic interactions to be of the order of $d/R_0 \simeq 10^{-3}$. This magnitude is not sufficient to cause a discontinuous transition between two different

neck sizes. Whether the interplay of these correction terms and the large effect caused by impurities can lead to such a discontinuous transition remains to be investigated.

Another possible explanation for the discrepancy could be that the pears with weak up–down asymmetry correspond to long-lived dynamical fluctuations around a metastable shape [39]. Indeed, one expects very long relaxation times near an instability since the time-scale $t_{\mathrm{f}} \equiv \eta R_0^3/\kappa$ for long-wave length bending fluctuations acquires an additional factor $1/(v_{\mathrm{c}} - v)$ near an instability at $v = v_{\mathrm{c}}$. Thus, the time-scale for a shape fluctuation towards the unstable mode t_{f} then formally diverges due to 'critical slowing-down'. In practice, this divergence will be cut-off by the decay of the metastable shape as soon as the energy barrier becomes comparable to the thermal energy T. On the basis of this estimate, the 'stable' pears would be long-lived fluctuations around a still metastable symmetric shape. Experiments to settle this issue are underway.

3.6. The equilibrium area difference as a possible control parameter

The equilibrium area-difference depends on the number of molecules in the two monolayers. If one assumes that the vesicles are relaxed with respect to the non-local bending energy right after they have been formed, i.e. $\Delta A = \Delta A_0$, the dimensionless equilibrium area-difference Δa_0 depends on the specific shape the vesicle acquired after closure. The difference between, e.g., a sphere and a capped cylinder leads to a difference of O(1) [38, 39]. Presently, the swelling process is not understood well enough to know which factors determine ΔA_0.

There are two effects which indicate that ΔA_0 can be modified by other factors than temperature. First, Fargé and Devaux [81] showed that redistributing lipids from one monolayer to another by applying a transmembrane ph-gradient induces shape transformations similar to those predicted theoretically as one increases ΔA_0. Secondly, the effect mentioned above that precooling leads to budding can, somewhat speculatively, also be related to changes in ΔA_0 using an intruiging suggestion by Helfrich and co-workers [82]. They proposed that osmotically enforced flow of water through the membrane drags along lipid molecules. Since precooling also forces solvent to flow through the membrane, one could wonder whether such a treatment also causes an increase in ΔA_0. In the phase diagram shown in fig. 10, this would shift the initial spherical vesicle upwards. A temperature trajectory starting at the sphere would then reach the budding line for a smaller temperature increase and the size of the buds should be smaller. So far, there are no systematic tests of this hypothesis. Obviously, quantitative experiments on the effect of the equilibrium area-difference will be very helpful in assessing whether the area-difference-elasticity model describes the main physics of these systems.

4. Shape fluctuations of quasi-spherical vesicles

4.1. Static amplitudes

Membranes are so flexible that they undergo thermally excited shape fluctuations which are visible in the microscope. The spectrum of these fluctuations depends on

the bending rigidity κ. Therefore, the analysis of the observed flickering of vesicles can be used to estimate κ as it will now be discussed for the case of quasi-spherical vesicles.

Quasi-spherical vesicles can be characterized by a fixed enclosed volume $V \equiv (4\pi/3)R_0^3$, which defines R_0 and a fixed internal ('true') area

$$A \equiv (4\pi + \Delta)R_0^2, \tag{27}$$

which defines the (dimensionless) excess area Δ. Note that in this section R_0 is defined by the enclosed volume rather than by the area as in the preceding sections. The fluctuating shape of a quasi-spherical vesicle can be parametrized as

$$R(\theta,\phi) = R_0\left(1 + \sum_{l\geqslant 0}^{l_{\max}} \sum_{m=-l}^{l} u_{l,m} Y_{lm}(\theta,\phi)\right), \tag{28}$$

where $|m| \leqslant l$, $u_{l,-m} = (-1)^m u_{l,m}^*$ and the functions Y_{lm} are the usual spherical harmonics.

The volume constraint fixes the amplitude $u_{0,0}$ as a function of the other amplitudes. The area constraint is difficult to incorporate exactly. It can be included in an approximative way by a Lagrangean multiplier term ΣA which is added to the energy W. If the area, A, and the bending energy, W, are expanded to second order in the amplitudes $u_{l,m}$, the result can be written as

$$A - 4\pi R_0^2 \approx R_0^2 \sum_{l\geqslant 2}^{l_{\max}} \sum_{m=-l}^{l} |u_{l,m}|^2 (l+2)(l-1)/2 \tag{29}$$

and

$$W + \Sigma A \approx \text{const} + (\kappa/2) \sum_{l\geqslant 2}^{l_{\max}} \sum_{m=-l}^{l} |u_{l,m}|^2 (l+2)(l-1)\big[(l+1)l + \sigma\big], \tag{30}$$

with the effective tension

$$\sigma \equiv \Sigma R_0^2/\kappa + \alpha(4\pi - \Delta A_0/4dR_0). \tag{31}$$

With the Boltzmann weight $\exp[-(W + \Sigma A)/T]$, one obtains the mean square amplitudes

$$\big\langle |u_{l,m}|^2 \big\rangle = (T/\kappa)\big[(l+2)(l-1)\big((l+1)l + \sigma\big)\big]^{-1}. \tag{32}$$

For $\alpha = 0$, i.e. without the area-difference elasticity but including a spontaneous curvature, the expressions (31) and (32) have been derived previously [45, 83, 84, 69]. The presence of the area-difference elasticity modifies the mean-square amplitudes whenever the equilibrium area difference ΔA_0 deviates from the optimal value for a

sphere ($16\pi dR_0$) as it will in general. However, this dependence is hidden together with the dependence on the Lagrangean multiplier in the effective tension σ.

The expressions for the mean square amplitudes (32) have been used to determine experimentally the bending rigidity κ from the contour fluctuations of quasi-spherical vesicles using phase contrast microscopy combined with fast image processing [45–50]. In this approach, σ is usually treated as a fit parameter for which one typically obtains values in the range $0 \lesssim \sigma \lesssim 100$.

Since the Lagrangean multiplier Σ has been introduced only to enforce the area constraint it should be eliminated in favor of the excess area Δ which is the physically meaningful quantity. Inserting the mean square amplitudes (32) into the expansion of the area (29) and comparing with the constraint (27) yields the implicit equation

$$\sum_{l\geqslant 2}^{l_{\max}} (2l+1)/\left(l^2+l+\sigma(\Delta)\right) = 2\Delta\kappa/T \equiv \delta \tag{33}$$

for σ. An analogous relation was first derived by Helfrich and Servuss for almost planar membranes [54]. The relation (33) shows that σ depends on the excess area only in the combination $\delta \equiv 2\Delta\kappa/T$. In general, (33) has to be inverted numerically to yield $\sigma = \sigma(\delta, l_{\max})$. If this inversion is performed approximately by replacing the sum with an integral one obtains

$$\sigma \simeq \frac{l_{\max}^2 + l_{\max} - 6\mathrm{e}^{\delta}}{e^{\delta} - 1}\,. \tag{34}$$

This relation shows that for $2\ln(l_{\max}/6) > \delta > 1$, the effective tension depends exponentially on the excess area. This effective tension is also called an *entropic* tension since it restricts the fluctuations of the individual modes by the area constraint.

After elimination of the effective tension the mean square amplitudes as given by (32) depend only on three quantities: (i) T/κ, (ii) the scaled excess area $\delta \equiv 2\Delta\kappa/T$, and (iii) the cutoff $l_{\max}$. They are independent of the equilibrium area difference ΔA_0 and the value of the non-local bending rigidity $\alpha\kappa$.

The temperature dependence of the mean square amplitudes provides an additional parameter which could become valuable for a more precise determination of the bending rigidity. To a first approximation, neither the cutoff $l_{\max}$, nor the bending rigidity should depend strongly on T in the narrow temperature range where the vesicle is quasi-spherical. However, the excess area depends quite dramatically on T. Assuming a constant thermal area expansion coefficient, β, i.e $A(T) = A(T_0)[1 + \beta(T - T_0)]$, we find

$$\Delta = 4\pi\beta(T - T_0), \tag{35}$$

where T_0 is the temperature where the excess area formally vanishes. With a typical value $\beta \simeq 5 \times 10^{-3}/^{\circ}\mathrm{C}$, a temperature change from $T = T_0 + 2\,^{\circ}\mathrm{C}$ to $T = T_0 + 7\,^{\circ}\mathrm{C}$ spans the range from 6 to 20 for δ, i.e. effective tensions σ ranging from 2500

to -5.3 (for $l_{\max} = 1000$). The entire set of measured mean square amplitudes at different temperatures should then all be described by the expressions (32), (33) and (35) using only T/κ, T_0 and $l_{\max}$ as fit parameters provided the quasi-spherical limit is applicable in the whole range. If the excess area Δ becomes too small, the fluctuations work against elastic expansion. If the area excess Δ becomes too large, the vesicle is no longer quasi-spherical but becomes prolate by a gradual crossover. For non-spherical shapes, the fluctuations have to be calculated numerically. So far, such a program has only been performed for discocyte shapes in an attempt to understand the flickering of red-blood-cells [85].

A similar reasoning would hold if the osmotic conditions were used to change the reduced volume of quasi-spherical vesicles. Again, the mean-square amplitudes should then be analysed as a function of the concentration of the osmotically active components.

4.2. Dynamics

The static mean-square amplitudes are, in principle, sufficient to determine the bending rigidity. However, more valuable information is contained in the dynamical behavior of these fluctuations. Since strong dissipation arises from the viscous damping in the surrounding fluid, these fluctuations are overdamped [86]. Within the spontaneous curvature model, Milner and Safran [69] based on work by Schneider et al. [45] derived the damping rates

$$\gamma_l = \frac{\kappa}{\eta R_0^3} \, \frac{l(l+1)(l+2)(l-1)((l+1)l + \sigma(\Delta))}{(2l+1)(2l^2+2l-1)}, \tag{36}$$

which show up in the dynamical correlation functions as

$$\left\langle u_{l,m}(t) u^*_{l,m}(0) \right\rangle = \left\langle |u_{l,m}|^2 \right\rangle \mathrm{e}^{-\gamma_l t}. \tag{37}$$

Here η is the viscosity of the surrounding medium. Measurements of the damping rates are indeed consistent with this prediction even though a detailed comparison is not yet feasible due to experimental limitations [49, 50, 87].

In this calculation, the bilayer architecture has been ignored. However, the analysis of the dynamical fluctuations of an almost planar bilayer membrane has shown, that the coupling between shape and density difference modifies the damping rates for wave-vectors q which are larger than a cross-over wave-vector q_1 [88]. For shorter wave-lengths, bending modes are so fast that the lipid density can no longer accommodate to the shape since intermonolayer friction provides an additional dissipative mechanism [89, 90]. This leads to a renormalization of the effective bending rigidity for shorter wave-length modes from κ to $\kappa + 2kd^2$ [88]. Rough estimates indicate that the cross-over vector q_1 corresponds to a wave-length in the μm-range. Even though the somewhat tedious calculation of this phenomenon in the quasi-spherical geometry has not yet been performed explicitly, one can expect significant deviations from the result (36) for wave-lengths smaller than this cross-over length due to the renormalization of the bending rigidity. In fact, because of the coupling between shape and lipid density, the correlation function decays no longer as a single exponential but rather involves two damping rates in this regime.

5. Non-spherical topology

5.1. Vesicles with one hole

5.1.1. Willmore problem, Clifford torus and conformal transformations

For vesicles of non-spherical topology [15, 91], an apparently simple theoretical problem remains to be solved [92]: What is the shape of minimal local bending energy

$$G \equiv (\kappa/2) \oint \mathrm{d}A(2H)^2 \tag{38}$$

among all shapes of given topology? For shapes of spherical topology, one can proof mathematically that the sphere is the absolute minimum. Willmore's conjecture gives a tentative answer for genus-1 vesicles, i.e. tori with one hole or, equivalently, shapes which are topologically equivalent to a sphere with one handle [92]. According to this conjecture, the shape of minimal bending energy is the Clifford torus which is an axisymmetric torus with circular cross-section and the ratio $\sqrt{2}$ between the two generating radii, see fig. 11. It has local bending energy $G = (\pi/2)8\pi\kappa$ and a reduced volume $v^* \simeq 0.71$.

A fundamental mathematical property of the local curvature energy G (38) is its invariance under conformal transformations in three-dimensional space [92]. In three dimensions, the group of conformal transformations contains inversions in a sphere apart from the trivial rotations, translations and scale-transformations. If such an inversion is applied to the Clifford torus, one obtains a one-parameter family of non-axisymmetric shapes which all have the same local curvature energy G but different reduced volume v in the range $v^* \leqslant v < 1$ [93, 94, 16]. A particular member of this family is also shown in fig. 11.

5.1.2. Phase diagram in the area-difference-elasticity model

As we have argued in section 2, the non-local bending energy is an important ingredient to describe the energy of vesicles more realistically. If this energy as well as the volume constraint is taken into account, the search for the shape of minimal

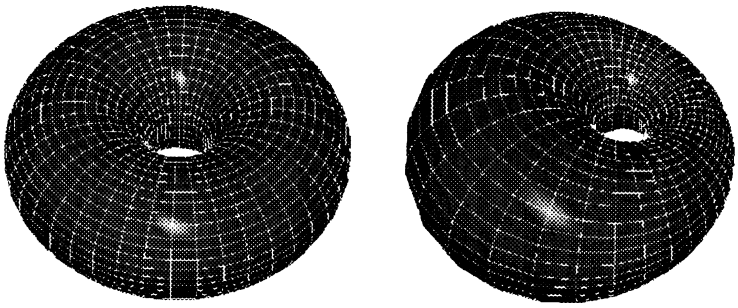

Fig. 11. Clifford torus (left) and a non-axisymmetric shape (right) obtained by a conformal transformation of this torus [16].

total energy becomes as complex as in the case of spherical topology. A detailed solution of this problem has been obtained by combining two methods. In a first step, the branches of stationary axisymmetric shapes of toroidal topology are determined [15, 16]. In a second step, the stability of these shapes is studied with respect to special conformal transformations [16].

A special conformal transformation consists of an inversion at the unit sphere, a translation about a vector **a** and a second inversion. Thus, any point **R** on the surface is mapped onto

$$\mathbf{R}' = \frac{\mathbf{R}/R^2 + \mathbf{a}}{|\mathbf{R}/R^2 + \mathbf{a}|^2}\,. \tag{39}$$

The advantage of such a mapping is that it can be treated perturbatively since it becomes the identity for small **a**. For an axisymmetric shape, the transformed shape will be non-axisymmetric, if the vector **a** is not parallel to the axis of symmetry. Therefore, the stability of the axisymmetric shapes with respect to a (particular) non-axisymmetric perturbation can be studied [95]. If, for a given set of parameters, the axisymmetric shape of minimal energy is found to be unstable, the groundstate must be nonaxisymmetric for these parameters. Even though one cannot expect to obtain the region of the non-axisymmetric ground states exactly, this method gives at least a lower bound on the extension of this region. This lower bound should be a reasonable approximation since it becomes exact in the neighborhood of the Clifford torus. The phase diagram obtained in this way within the area-difference-elasticity model together with some representative shapes is shown in fig. 12 [16]. The main feature is the large region of non-axisymmetric shapes which are separated from the axisymmetric shapes by the instability line C^*.

5.1.3. Experiments

The different types of toroidal shapes as observed experimentally by Bensimon and co-workers [18] can indeed be located in the phase diagram. (i) The axisymmetric circular torus with an estimated reduced volume of $v \simeq 0.5$ [18] fits well into the phase diagram since circular shapes with $v = 0.5$ exist within a large range of Δa_0. (ii) The observed non-axisymmetric torus with $v \simeq 0.77$ [18] resembles the non-axisymmetric shape shown in fig. 11. Indeed, the phase diagram of the area-difference-elasticity model shows that shapes with $v \simeq 0.77$ are definitely non-axisymmetric for all Δa_0. (iii) Mostly Clifford tori have been observed in the first experimental study of genus-1 tori where the lipid was partially polymerized [96].

For a crucial test of the theory, one parameter such as temperature should be varied in a systematic way. A temperature trajectory passing through a circular torus at low reduced volume and a non-axisymmetric torus at large reduced volume is also shown in fig. 12. Thus, the model predicts that for any circular torus a decrease in temperature will lead to a non-axisymmetric torus via a continuous shape transformation which indeed has been verified experimentally [19].

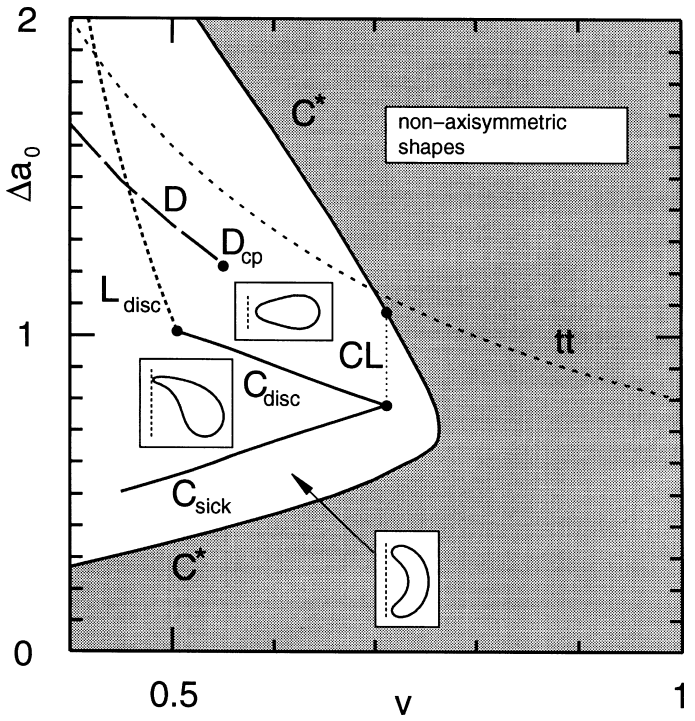

Fig. 12. Phase diagram for tori in the area-difference-elasticity model with rigidity ratio $\bar{\kappa}/\kappa = \alpha = 1$ as a function of the equilibrium area-difference Δa_0 and of the reduced volume v. Three axisymmetric regions which are separated by continuous shape transformation lines $C_{\rm sick}$ and $C_{\rm disc}$ can be distinguished: (i) discoid tori, (ii) sickle-shaped tori and (iii) toroidal stomatocytes. Within each region, a typical contour is shown. The line $L_{\rm disc}$ represents limit shapes with vanishing hole diameter. The instability with respect to axisymmetry breaking conformal transformations is denoted by C^*. Within the region of axisymmetric shapes with a reflection plane, discontinuous shape transformations from circular tori to discoid tori occur along the line D which ends in the critical point $D_{\rm cp}$. The Clifford torus is the shape of minimal energy along the dotted line CL. A temperature change corresponds to a temperature trajectory as indicated by the dashed line (tt). This trajectory crosses the line C^* which implies that axisymmetry breaking shape transformations of toroidal vesicles can be induced by temperature changes [16].

5.2. Shapes with more holes or handles

5.2.1. Phase diagram and conformal diffusion for genus 2

Vesicles with more than one hole or handle are necessarily non-axisymmetric. This makes the calculation of such shapes much more difficult than for the cases considered so far. Fortunately, the combination of a mathematical conjecture, conformal transformations, and numerical methods provide much insight into the phase diagram.

For genus-2 vesicles, i.e. vesicles with two holes or handles, Kusner conjectured that the Lawson surface as shown in fig. 13 minimizes the local bending energy [97]. Applying conformal transformations to this Lawson surface generates a three-dimensional space of shapes with the same energy [17, 98, 99].

For real vesicles, the constraints on the reduced volume as well as the presence of

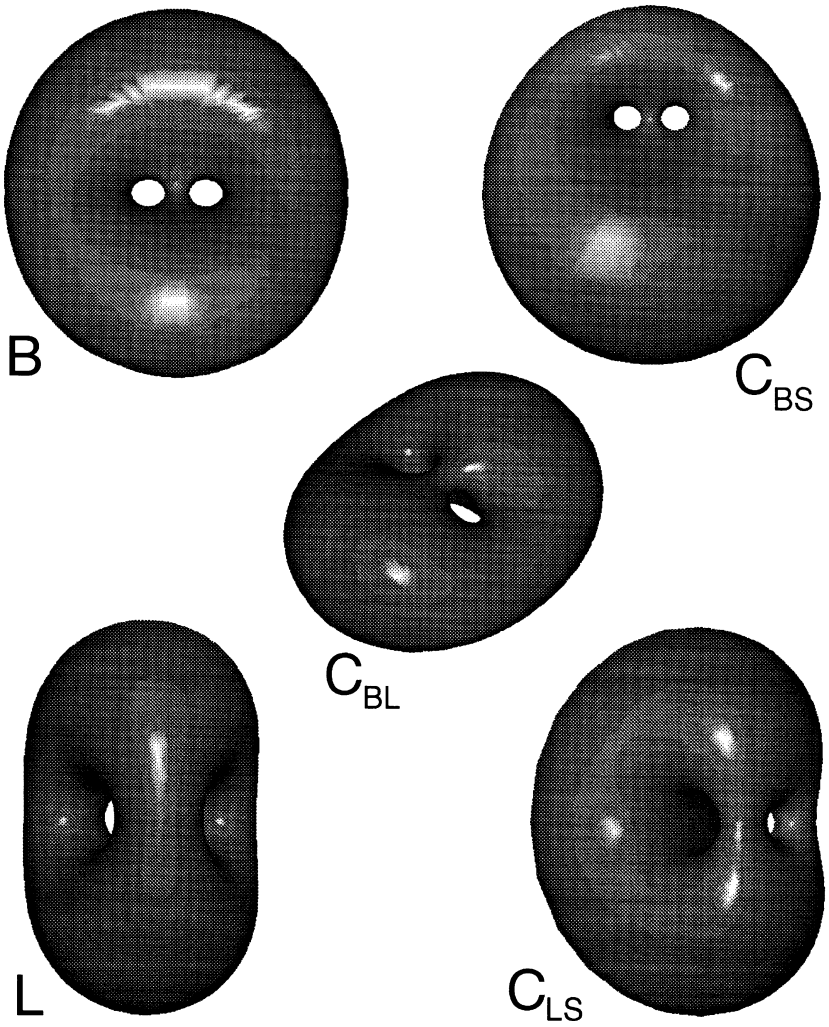

Fig. 13. Lawson surface (L) and some of its conformal transformations, where B denotes the button surface. The letters refer to the location of these shapes in the phase diagram shown in fig. 14 [17].

the non-local bending energy 'eliminate' two dimensions of this degeneracy. However, there still remains a one-parameter family of shapes which all have the same reduced volume and the same total bending energy [17, 99]. For genus-2 vesicles, there is a whole region in the phase diagram where the ground state is degenerate as shown in fig. 14.

In this region, theory predicts a diffusion process in shape space along a conformal mode which neither changes the reduced volume nor the total mean curvature [17, 99]. An example of such a conformal diffusion process is shown in fig. 15. Within the parameter space region W, the typical diffusion time in the shape space

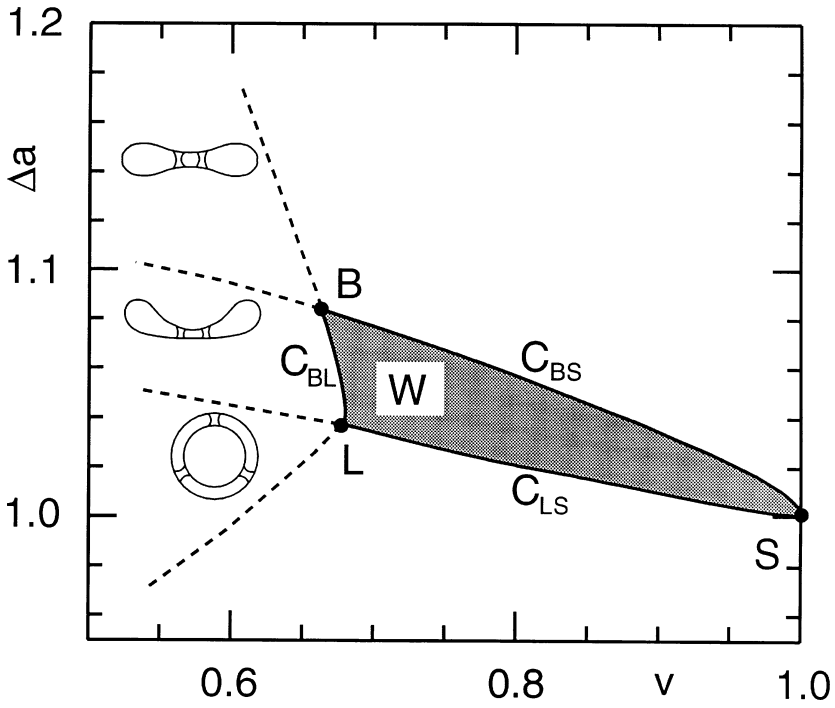

Fig. 14. Phase diagram for genus-2 vesicles as a function of the reduced volume v and the area difference Δa. Within the region W, the ground state is conformally degenerate. This region is bounded by the lines $C_{\rm BS}$, $C_{\rm BL}$ and $C_{\rm LS}$. The Lawson surface L and the button surface B are special points at the boundary of W. The shape S denotes the sphere with two infinitesimal handles. Adjacent to W, five different regions exist. Cartoons characterize the shapes within three of these five regions [17].

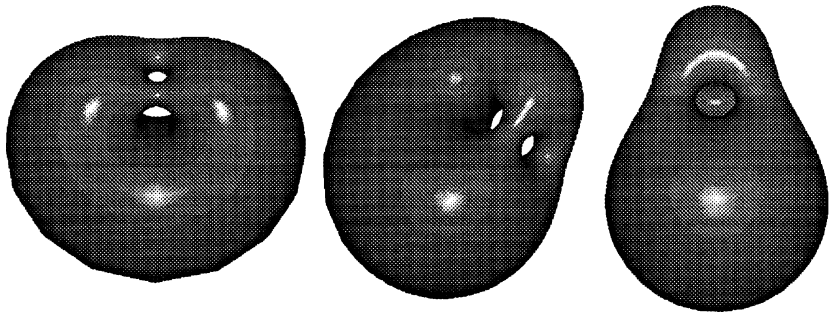

Fig. 15. Shapes along a conformal diffusion mode. All three shapes have the same curvature energy, the same reduced volume and the same reduced area-difference. Both the left and the right shape are the two special shapes along this conformal mode which possess one symmetry plane, while the shape in the middle has no symmetry plane [17].

should be of the order of $t_{\rm cf} = \eta R_0^3/T$ for a solvent of viscosity η at temperature T, as follows from dimensional analysis. This time-scale is significantly longer than the time-scale $t_{\rm b} = \eta R_0^3/\kappa$ for long-wave-length bending fluctuations since $\kappa/T \simeq 25$ for phospholipid membranes. Since the existence of the phase W is strongly dependent on the specific form of the bending energy, the observation of conformal diffusion would directly confirm this form. Higher order corrections to the energy (11) which are of the order of $\sim d/R_0 \simeq 10^{-3}$ are small compared to a thermal energy T and thus should not suppress conformal diffusion.

Outside of W, the shapes of minimal energy have a larger energy than the Lawson surface. Cartoons of these shapes which have at least two symmetry planes are also shown in the phase diagram of fig. 14.

5.2.2. Higher genus

Conformal diffusion will be generic for higher genus vesicles since regions with conformally degenerate ground state exist for any genus $g \geqslant 2$. For $g > 2$, the local bending energy without any constraint possesses even more than one stationary shape [100, 98] Consequently, there will be several regions of one-dimensional degenerate ground states for higher genus vesicles. Discontinuous transitions together with regions of metastability are then likely to occur.

5.2.3. Experiments

Genus-2 vesicles have recently been observed experimentally. First, a button-like shape has been found [18]. It can be directly located in the phase diagram for genus-2 shapes shown in fig. 14. According to the theory, a ground state with three symmetry planes cannot belong to the degenerate phase. Consequently, this shape does not belong to the degenerate phase W and should not exhibit conformal diffusion in agreement with the observation. Starting from this button surface a decrease in temperature will increase v which should eventually lead into the phase W. The onset of conformal diffusion should then be observed as soon as the temperature trajectory crosses the boundary to the region W.

The second type of genus-2 shapes observed so far [101] resembles the phase with threefold symmetry in the lower left corner of the phase diagram. For small v, these shapes consist of two concentric spheres connected by narrow necks. The position of these necks shows strong fluctuations. Even though one does not expect conformal diffusion for these shapes to happen, the pronounced fluctuations indicate that there are shape excitations of low energy for these shapes. In fact, in the limit of small v, the effective interaction between the necks vanishes [101]. The same type of shapes with more than three necks has also been observed [101].

Finally, recent experiments show strongly fluctuating shapes which could be interpreted as conformal diffusion [19]. However, it is difficult to distinguish experimentally rotational diffusion from conformal diffusion since only a two-dimensional cut of the three dimensional shape can be observed. More experiments are certainly needed in order to obtain more information on these diffusion processes.

6. Lipid mixtures

6.1. Fluid membranes consisting of several components

In general, a lipid bilayer is composed of different types of molecules which may differ in their head groups, in the length of their hydrocarbon chains or in the number of unsaturated bonds within these chains. In such a multi-component system, the composition can become laterally inhomogeneous within each monolayer and can be different across the two monolayers. As a result, the elastic parameters of the membrane such as the bending rigidity and the spontaneous curvature become inhomogeneous which leads to a coupling between the composition and the shape. Moreover, there are energies associated with the composition variables such as entropy of mixing and the cost of an inhomogeneous composition profile. To categorize the various phenomena which arise from the competition between these energies and the curvature energy, it is helpful to distinguish two cases based on the phase diagram of a multi-component bilayer.

Usually, the phase diagram of a multicomponent bilayer exhibits a homogeneous one-phase region at high temperature and a two-phase coexistence region at lower temperatures for a certain range of compositions.

(i) In the two-phase region, domains for which the lipid composition is different from the surrounding matrix are formed [102, 103]. The edges of these domains are characterized by an edge or line tension. Since the length of the domain boundary decreases if the domain buds, the competition between this edge tension and the curvature energy leads to *domain-induced budding* [12, 60, 104]. This budding process is discussed in section 6.2 both for a flat membrane matrix and for vesicles.

Quite generally, these domains seem to be an essential feature of the spatial organization of biological membranes. For example, the plasma membranes of most cells contain specialized regions such as coated pits or various types of cell junctions. These domains represent an important theme of current research in structural biology [105].

(ii) In the one-phase region, the groundstate is a flat and laterally homogeneous membrane in the absence of a spontaneous curvature. However, any inhomogeneity in the composition, either laterally within a monolayer or between the two monolayers, induces a local spontaneous curvature if the two lipid species have a different molecular geometry. For an almost planar membrane, this leads to a coupling between bending fluctuations and composition fluctuations which decreases the bending rigidity [106, 107]. For a non-spherical vesicle, this coupling between shape and composition causes *curvature-induced lateral phase segregation* [13] as discussed in section 6.3.

In the following, we focus on fluid lipid bilayers. Even though the mixture of two lipid components often leads to the coexistence of a fluid and a gel phase, there are several examples for the coexistence of two fluid phases. An especially important one is provided by mixtures of phospholipids and cholesterol as has been established quite recently [108, 109, 110]. Fluid-fluid coexistence also occurs in the binary mixture of DEPC and DPPE [111] and in mixtures with partially unsaturated alcyl chains [112].

Domain-induced budding and curvature-induced phase segregation as considered here must be distinguished from related but different phenomena such as striped phases [113, 114], spontaneous formation of small vesicles in mixtures of oppositely charged surfactants where phase separation occurs across the membrane [115–118], and shape transformations induced by a coupling between a local in-plane order and the membrane normal for smectic-C vesicles [119].

6.2. Domain-induced budding

6.2.1. Phase separation within bilayers

The two coexisting phases of the lipid mixture will be denoted by α and β. This ($\alpha\beta$) two-phase region exhibits (i) a nucleation regime, in which one has to overcome an energy barrier in order to form a 'critical' domain, and (ii) a regime of spinodal decomposition in which such a barrier is absent.

Now, consider a membrane which is initially prepared in a homogeneous state within the one-phase region and is then quenched into the ($\alpha\beta$) two-phase region. This leads to phase separation within the membrane which can proceed in two different ways depending on the 'depth' of the quench: (i) The membrane is quenched deep into the spinodal decomposition regime. In such a situation, many small domains will be formed initially which may then undergo the usual coarsening process of spinodal decomposition. At this stage, the morphology of the domains and of their boundaries may be quite complex. At later stages, on the other hand, the coarsening process should be dominated by a few large domains the size of which grows as $t^{1/3}$ with time t. In this way, one may finally attain a state of complete phase separation in which the bilayer consists of two large domains. (ii) The membrane is quenched into the nucleation regime. If the activation energy for the 'critical' domain is sufficiently large, only one domain will be nucleated initially and one may study the diffusion-limited growth of such a single domain.

6.2.2. Edge energy and line tension

The edge of an intramembrane domain has an energy which is proportional to the edge length. Therefore, the domain has a tendency to attain a circular shape in order to minimize its edge energy.

The line tension, Σ_{e}, is equal to the edge energy per unit length. Its magnitude can be estimated as follows [12]. First, consider a domain in the lipid bilayer which extends across both monolayers. In this case, the edge of the domain represents a cut across the whole bilayer. The cross-section of such a cut consists of three distinct regions: two hydrophilic headgroup regions of combined thickness $\simeq 1$ nm and an intermediate hydrophobic tail region of thickness $\simeq 4$ nm. These two regions can have distinct interfacial free energies per unit area. For 3-dimensional fluid phases, a typical value for the interfacial free energy is $\simeq 10^{-2}$ Jm^{-2}. If one assumes that this value is also applicable to the headgroup region and that the latter region gives the main contribution to the line tension, one obtains the crude estimate $\Sigma_{\mathrm{e}} \simeq 10^{-17}$ J/μm. For a domain which extends only across one monolayer, the line tension is reduced by a factor $1/2$. For monolayers composed of a phospholipid-cholesterol mixture, experimental studies of the domain shape gave the estimate $\Sigma_{\mathrm{e}} \simeq 10^{-18}$ J/μm [120].

6.2.3. Egde energy versus bending energy

A *flat* domain will form a circular disk in order to attain a state with minimal edge length. For a circular domain with radius L, the edge energy, $F_{\rm e}$, is given by

$$F_{\rm e} \equiv 2\pi L \Sigma_{\rm e}. \tag{40}$$

However, as far as the edge energy is concerned, a *flat* circular disk does *not* represent the state of lowest energy since the length of the edge can be further reduced if the domain forms a bud: the domain edge now forms the neck of the bud, and this neck narrows down during the budding process, see fig. 16.

Budding involves an increase in the curvature and thus in the bending energy of the domain. Therefore, the budding process of fluid membranes is governed by the competition between the bending rigidity κ of the domain and the line tension $\Sigma_{\rm e}$ of the domain edge. This competition leads to the characteristic *invagination length*, $\xi \equiv \kappa/\Sigma_{\rm e}$ [12]. Using the typical values $\kappa \simeq 10^{-19}$ J and $\Sigma_{\rm e} \simeq 10^{-17}$ J/μm, one obtains $\xi \simeq 10$ nm for domains across the bilayer. For phospholipid-cholesterol mixtures, this length scale seems to be much larger. On the one hand, the bending rigidity κ was experimentally estimated to have the relatively large value $\kappa \simeq 4 \times 10^{-19}$ J [49]. The line tension, on the other hand, seems to have the relatively small value $\Sigma_{\rm e} \simeq 10^{-18}$ J/μm as mentioned above. This implies the invagination length $\xi \simeq 400$ nm. It will become clear in the following that the invagination length ξ provides the natural length scale for shape transformations of the domain.

6.2.4. A simple model

The competition between the edge and bending energies can be understood in the framework of a relatively simple model in which one assumes that the membrane

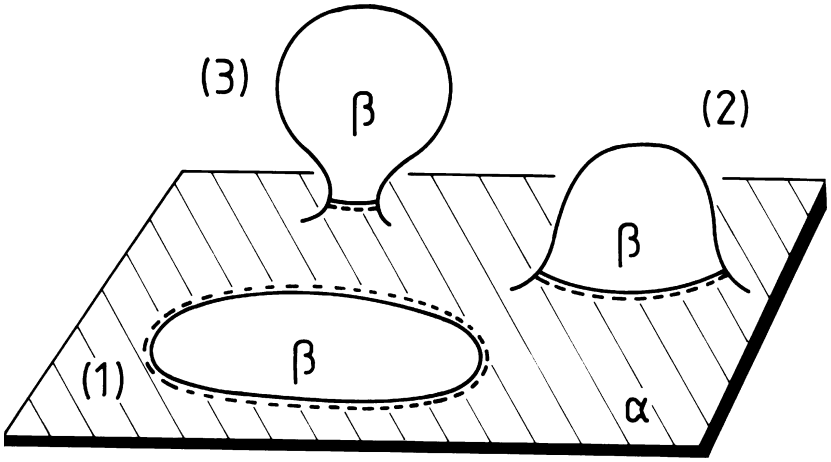

Fig. 16. Budding of the membrane domain β embedded in the membrane matrix α. The domain edge is indicated by the full-broken line. The length of this edge decreases during the budding process from (1) to (3) [12].

matrix is flat and that the membrane domain forms a spherical cap with radius R. If the domain has surface area $A = \pi L^2$, mean curvature $C = 1/R$, and spontaneous curvature $C_{\rm sp} = C_0/2$, its total energy $F = F_{\rm SC} + F_{\Sigma_{\rm e}}$ has the form

$$F/2\pi\kappa = (LC - LC_{\rm sp})^2 + (L/\xi)\sqrt{1 - (LC/2)^2}. \tag{41}$$

For $C_{\rm sp} = 0$, such a model has also been studied in order to discuss the size of vesicles generated by sonification and to study the closure of open fluid membranes [121–123]. The energy F has several minima and maxima as a function of the reduced curvature LC. There are always two boundary minima at $LC = \pm 2$ corresponding to complete spheres on both sides of the membrane. The complete sphere with the lower energy will be called the *complete bud*. For zero spontaneous curvature, both complete spheres have the same energy, and the complete bud can develop equally well on both sides. A finite value of $C_{\rm sp}$ breaks this symmetry, and budding occurs preferentially on one side of the membrane. For small values of L/ξ, the energy F exhibits another minimum at intermediate values of LC. This minimum corresponds to the *incomplete bud*. For $C_{\rm sp} = 0$, this minimum is at $LC = 0$, and the incomplete bud is flat.

Now, consider a domain which is characterized by fixed spontaneous curvature $C_{\rm sp}$ and fixed invagination length $\xi = \kappa/\Sigma_{\rm e}$. The domain size L, on the other hand, changes with time by the diffusion-limited aggregation of molecules within the membrane and thus plays the role of a control parameter for the budding process.

For small L, the domain forms an incomplete bud corresponding to the minimum of F at small LC-values. As L grows, the edge of the domain becomes longer, and the energy of the incomplete bud is increased. At a certain critical size, $L = L^*$, the incomplete and the complete bud have the same energy but are separated by an energy barrier. For the parameter values considered here, the energy barrier is typically large compared to the thermal energy $\simeq T$. In this case, the domain continues to grow in the incomplete bud state up to the limiting size $L = L^0$ at which the energy barrier disappears and this state becomes *unstable*. The simple model considered here leads to [12]

$$L^0 = 8\xi/\left[1 + \left(4\xi|C_{\rm sp}|\right)^{2/3}\right]^{3/2} \tag{42}$$

with $\xi = \kappa/\Sigma_{\rm e}$ as before. Thus, as soon as the domain has grown up to $L = L^0$, it *must* undergo a budding process.

6.2.5. Domain-induced budding of vesicles

The same type of shape instability is found from a systematic minimization procedure for the energy of closed vesicles composed of two types of domains, α and β [60]. This energy consists (i) of the bending energies $F_{\rm SC}^{(\alpha)}$ and $F_{\rm SC}^{(\beta)}$ of the α and the β domains, respectively, and (ii) of the edge energy $F_{\rm e}^{(\alpha\beta)}$ of the $(\alpha\beta)$ domain boundaries:

$$F = \oint {\rm d}A^{\alpha}\ \frac{1}{2}\,\kappa^{\alpha}(2H - 2\ C_{\rm sp}^{\alpha})^2 + \oint {\rm d}A^{\beta}\ \frac{1}{2}\,\kappa^{\beta}(2H - 2\ C_{\rm sp}^{\beta})^2 + \oint {\rm d}\ell\ \Sigma_{\rm e} \tag{43}$$

as appropriate for a surface consisting of α and β domains where the last integral represents the line integrals along the domain boundaries.

The total energy F is minimized for given values of the domain areas A^α and A^β, of the pressure difference P or of the enclosed volume V, and of the line tension $\Sigma_{\rm e}$. The area ratio

$$x \equiv A^\beta/\left(A^\alpha + A^\beta\right) \tag{44}$$

with $0 \leqslant x \leqslant 1$ is a measure for the size of the domain and again plays the role of a control parameter for budding.

The minimization of the energy functional does not determine the boundary conditions at the domain boundary completely. This freedom corresponds to different ways to model the domain boundary. Two extreme cases are (i) that the domains α and β can meet at any angle with no difference in energy, and (ii) that the surface has to be smooth at the domain boundary. The most physical assumption seems to be case (ii), for which both domains meet with the same angle. This boundary condition has been used in ref. [60].

6.2.6. Equilibrium shapes of vesicles with two domains

First, assume that the vesicle contains two large domains, α and β, the size of which does no longer change with time. This corresponds to the final state after the phase separation process has been completed. On long timescales, water can permeate through the membrane which leads to zero pressure difference, $P = 0$, provided the aqueous solution does not contain large molecules which lead to an osmotic pressure.

The equilibrium shapes of such a vesicle are shown in fig. 17. For simplicity, the α and the β domain are taken to have identical bending rigidities, $\kappa^\alpha = \kappa^\beta$, and to have no spontaneous curvature, i.e. $C^\alpha_{\rm sp} = C^\beta_{\rm sp} = 0$.

As shown in fig. 18, the corresponding phase diagram exhibits a line $D_{\rm bud}$ of discontinuous budding transitions and a line $L_{\rm cb}$ of limit shapes with an infinitesimal

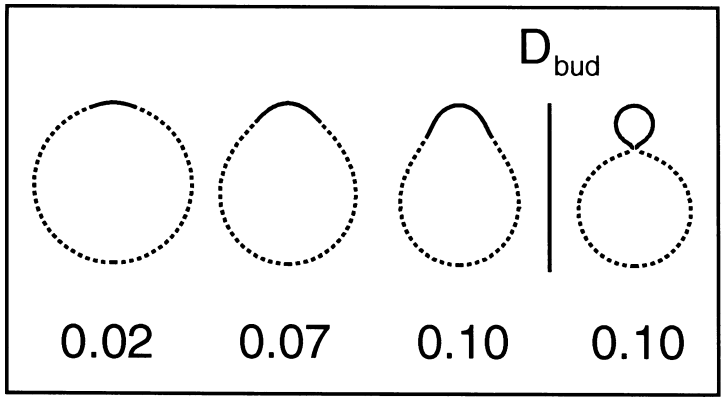

Fig. 17. Vesicle shapes as a function of the relative domain area x for reduced line tension $\sigma_{\rm e} = 7$. $D_{\rm bud}$ denotes a discontinuous transition between an incomplete and a complete bud. The shapes are axisymmetric; the α and the β domain correspond to the broken and the full contour, respectively [60].

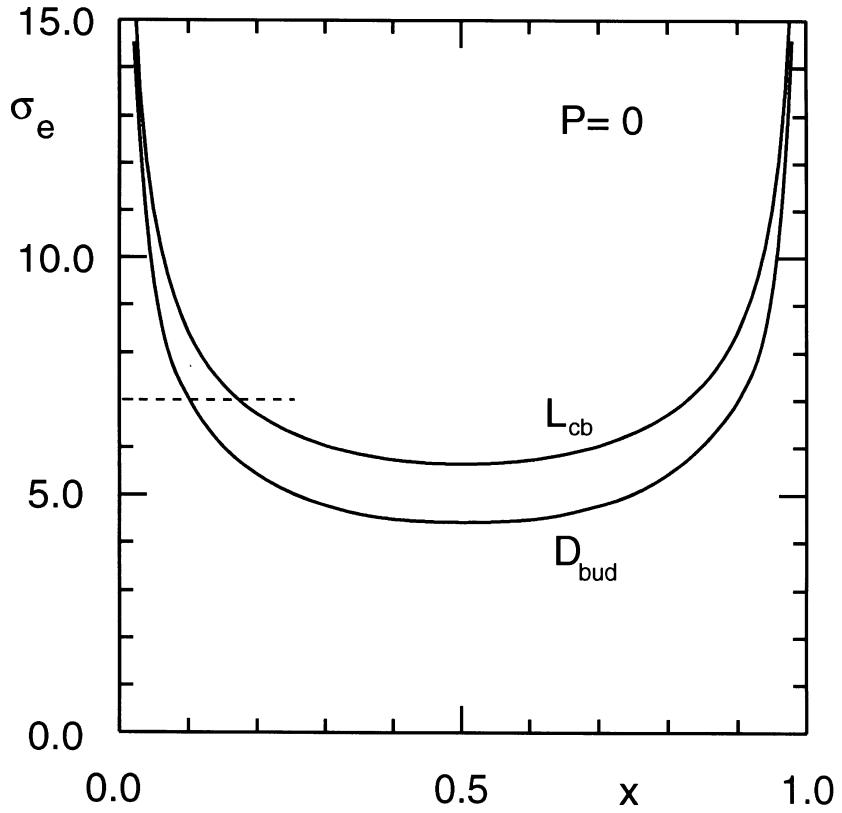

Fig. 18. Phase diagram for domain-induced budding of a vesicle for pressure $P = 0$ across the membrane as a function of the reduced line tension $\sigma_{\rm e}$ and the relative domain area x. The vesicle undergoes a discontinuous budding transition along the line $D_{\rm bud}$, and attains a limit shape at $L_{\rm cb}$ with an infinitesimal neck connecting the bud to the vesicle. The dashed trajectory corresponds to fig. 17 [60].

neck. The dashed line in fig. 18 corresponds to a vesicle with reduced line tension $\sigma_{\rm e} = 7$ where

$$\sigma_{\rm e} \equiv \Sigma_{\rm e} R_0/\kappa^\beta = R_0/\xi. \tag{45}$$

The corresponding energy and equilibrium shapes are shown in fig. 17 as a function of x. In practice, the infinitesimal neck should have a diameter which is of the order of the membrane thickness, $a \simeq 5$ nm. The energy required to break such a neck is $2\pi a \Sigma_{\rm e}$ and the time for thermally-activated fission is $\sim \exp(2\pi a \Sigma_{\rm e}/T)$.

If the vesicle membrane is composed of a phospholipid-cholesterol mixture, the invagination length seems to be $\xi \simeq 400$ nm as mentioned above, and the sequence of shape transformations shown in fig. 17 would then correspond to the vesicle size $R_0 = 7\xi \simeq 2.8$ μm which is directly accessible to optical microscopy.

6.2.7. Growth of nucleated domain

Secondly, consider a vesicle with reduced volume $v = 3V/4\pi R_0^3 < 1$ which has been prepared by a quench from the one-phase region of the bilayer into the nucleation regime of its two-phase coexistence region. After such a quench, the bilayer remains in its homogeneous phase, say α, until a domain of the minority phase, say β, has been nucleated. The β domain will then grow by diffusion-limited aggregation within the α matrix and the relative surface area $x = A^\beta/A$ will increase in time.

For each value of x, one may determine the shape of lowest energy. In fig. 19, the corresponding phase diagram is shown for a prolate vesicle with $v = 0.8$ as a function of x and of the reduced line tension σ_e for domains with identical bending rigidities and zero spontaneous curvature.

As x is increased, the prolate vesicle undergoes a discontinuous budding transition denoted by D_{bud} provided $\sigma_e > \sigma_{e,c} \simeq 9.7$. As x is further increased, the bud closes its neck and forms a limit shape at L_{cb}. Comparison of fig. 19 and fig. 18 shows

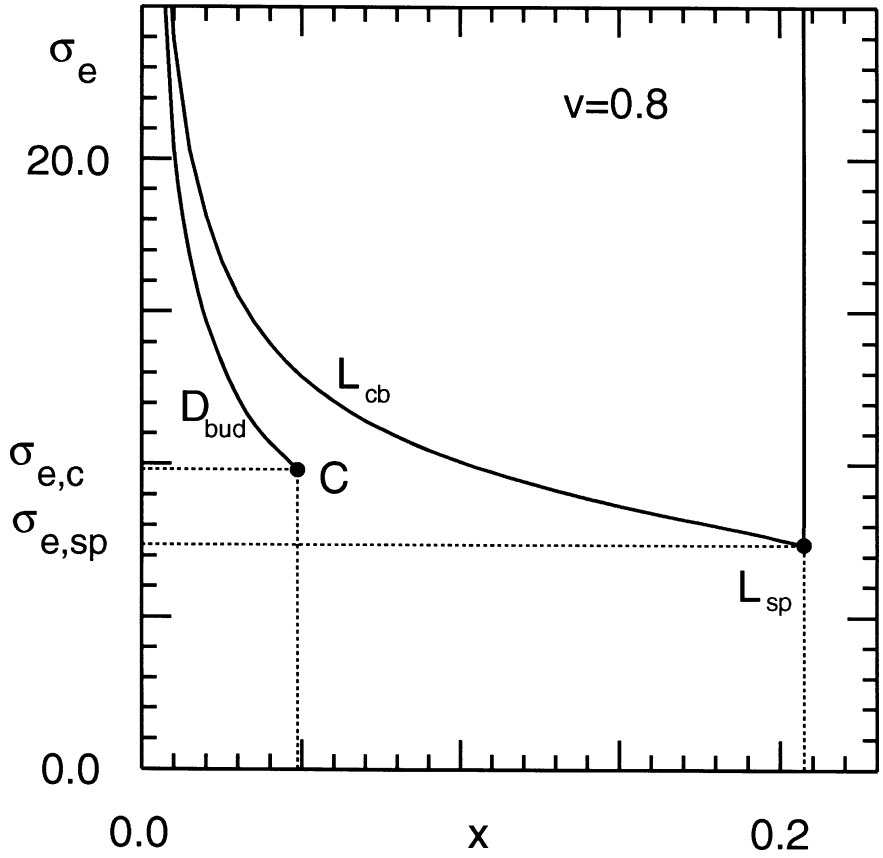

Fig. 19. Phase diagram of domain-induced budding of a prolate vesicle with constant enclosed volume $v = 0.8$ as a function of the reduced line tension σ_e and the relative domain area x. The line D_{bud} of discontinuous budding transitions ends in the critical point C [60].

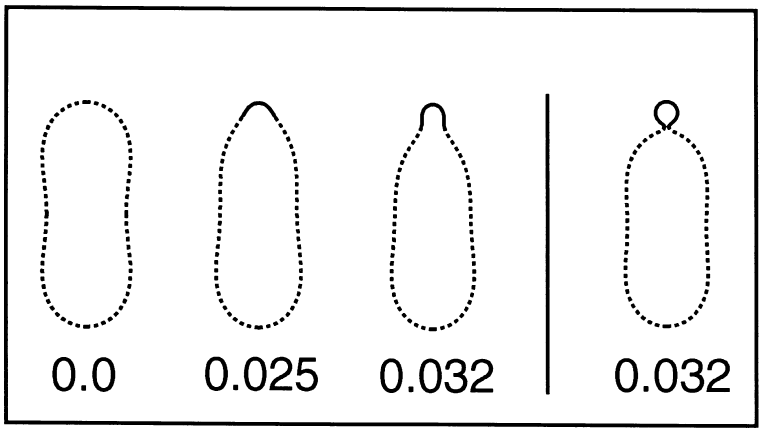

Fig. 20. Equilibrium shapes for different values of the relative domain area x and reduced line tension $\sigma_e = 12$. The incomplete bud represents a metastable state up to $x = 0.032$ where it becomes unstable and decays into the complete bud [60].

that the volume constraint truncates the line of discontinuous budding transitions at a critical point $(x, \sigma_e) = (x_c, \sigma_{e,c}) \simeq (0.5, 9.7)$ at which the budding transition is continuous. For $\sigma_e < \sigma_{e,c}$, there is no sharp budding transition. For $\sigma_e < \sigma_{e,sp} \simeq 7.4$, no limit shape with infinitesimal neck can be attained and no budding occurs. The shape transformation of the prolate vesicle with $\sigma_e = R_0/\xi = 12$ is shown in fig. [20].

6.2.8. Generalized neck condition

The complete bud can have a neck with a finite diameter. This neck diameter decreases further with the growth of the domain until the neck closes completely as the limit shape L_{cb} has been attained. In the absence of the volume constraint, this limit shape consists of two spheres, one α and one β sphere, separated by an infinitesimal neck which contains the domain boundary. These limit shapes can be characterized by the generalized neck condition [60]

$$\kappa^\alpha/R^\alpha + \kappa^\beta/R^\beta = \kappa^\alpha C^\alpha_{sp} + \kappa^\beta C^\beta_{sp} + \frac{1}{2}\,\Sigma_e. \tag{46}$$

Here, $1/R^\alpha$ and $1/R^\beta$ are the curvatures of the two domains at the point where they meet to form the ideal neck. If $C^\alpha_{sp} = C^\beta_{sp}$, $\kappa^\alpha = \kappa^\beta$ and $\Sigma_e = 0$, one recovers the ideal neck (or kissing) condition $1/R^\alpha + 1/R^\beta = 2C_{sp}$ for the homogeneous case as given by (17). For domains with identical bending rigidities and zero spontaneous curvature, the neck condition $1/R^\alpha + 1/R^\beta = \Sigma_e/(2\kappa)$ shows that the line tension Σ_e plays a role very similar to the spontaneous curvature. The neck condition (46) completely determines the lines L_{cb} of limit shapes in the phase diagram.

6.3. Curvature-induced lateral phase segregation

6.3.1. Coupling between composition and shape

Even if there is no genuine phase separation in the flat membrane, the shape transformation of the closed vesicle can induce phase segregation within the membrane [13]. Suppose an initially spherical vesicle is subject to a temperature increase. This change necessarily leads to deviations from the spherical shape and, thus, to a position-dependent curvature which induces a position-dependent composition. For a quantitative description, we introduce the composition (area fractions) of lipid A in the individual monolayers $x_{\rm A}^{\rm i}(= 1 - x_{\rm B}^{\rm i})$ (i $=$ in, out) and deviations $\delta x_{\rm A}^{\rm i}(s_1, s_2) \equiv x_{\rm A}^{\rm i}(s_1, s_2) - \bar{x}_{\rm A}$, from the mean value $\bar{x}_{\rm A}$. If this local deviation is different in the two monolayers, a local spontaneous curvature is induced according to

$$C_0(s) = \lambda\big(\delta x_{\rm A}^{\rm out}(s) - \delta x_A^{in}(s)\big) + \overline{C}_0 \equiv \lambda\phi(s) + \overline{C}_0, \tag{47}$$

where the phenomenological coupling constant λ has the dimensions of an inverse length [106]. For a rough estimate of its magnitude, assume that the lipid A has a cone-like shape with a radius of curvature $R_{\rm A}$ while lipid B has a cylindrical shape. The coupling constant λ is then of the order of $1/R_{\rm A}$. Since $R_{\rm A}$ is determined by typical molecular dimensions, we will use $\lambda = 1/10$ nm for a conservative estimate. We also allow for a systematic spontaneous curvature $\overline{C}_0$ which arises if the mean compositions $\bar{x}_{\rm A}^{\rm i}$ are different in the two monolayers.

6.3.2. Energy of a two-component vesicle

The bending energy, F_1, of the two-component vesicle is then chosen as a generalization of the bending energy of a single-component vesicle as given by (11). This leads to [13]

$$\begin{aligned} F_1 = (\kappa/2) \oint {\rm d}A\big[2H(s_1, s_2) - C_0\big(\phi(s_1, s_2)\big)\big]^2 \\ + \big[\pi\bar{\kappa}/\big(8Ad^2\big)\big](\Delta A - \Delta A_0)^2. \end{aligned} \tag{48}$$

We have assumed for simplicity that neither the bending rigidities κ and $\bar{\kappa}$ nor the area of the vesicle, A, and area-difference ΔA_0 depend on the composition.

Since the membrane does not show genuine phase separation, there is a free energy associated with the deviation of the composition from its mean value. For small deviations, this energy can be written in the form

$$F_2 = (\kappa/2)\varepsilon \oint {\rm d}A\big[\phi^2 + (\xi_{\rm c}\nabla\phi)^2\big]. \tag{49}$$

Here, $\xi_{\rm c}$ is the correlation length for composition fluctuations, ∇ is the covariant gradient operator and ε is a molecular energy, estimated below, divided by the bending rigidity.

Since the typical length-scale for shape variations of large vesicles is in the micrometer-range, while the typical correlation length ξ_c will be of the order of nanometers, the gradient term in F_2 will be, in general, much smaller than the ϕ^2-term and, thus, can be ignored. Under the constraint $\oint \mathrm{d}A\phi = 0$, the total energy, $F \equiv F_1 + F_2$, then becomes minimal for a composition profile $\phi(s_1, s_2)$ given by

$$\phi(s_1, s_2) = \frac{2\lambda}{\lambda^2 + \varepsilon} \left[H(s_1, s_2) - \Delta A/(4dA) \right], \tag{50}$$

which shows that the local composition follows the deviation of the mean curvature $H(s_1, s_2)$ from its average value $\Delta A/(4dA)$. After inserting (50) into F, the total energy can be written as

$$F = \frac{\kappa}{2\delta} \left\{ \oint \mathrm{d}A \; (2H)^2 + \left[\pi\bar{\kappa}_{\mathrm{eff}}/\left(4\kappa A d^2\right) \right] (\Delta A - \Delta A_{0,eff})^2 + \mathrm{const} \right\}. \tag{51}$$

This expression is the standard form of the bending energy of a single-component vesicle in the area-difference-elasticity model in which the three model parameters have been renormalized. First, the effective bending rigidity is κ/δ where

$$\delta \equiv 1 + \lambda^2/\varepsilon > 1 \tag{52}$$

measures the effective strength of the curvature to composition coupling. Thus, the bending rigidity decreases for a two-component system, as has been previously derived [106]. Secondly, the non-local term becomes more relevant for stronger couplings since the non-local bending rigidity is renormalized according to

$$\bar{\kappa}_{\mathrm{eff}} \equiv \bar{\kappa} + (\delta - 1)(1 + 1/\pi)\kappa > \bar{\kappa}. \tag{53}$$

Finally, the renormalized equilibrium area difference is

$$\Delta A_{0,\mathrm{eff}} \equiv (\kappa/\bar{\kappa}_{\mathrm{eff}}) \left(2\overline{C}_0 dA_0/\pi + \bar{\kappa}\Delta A_0/\kappa \right). \tag{54}$$

Once this mapping has been obtained, both the knowledge of the phase diagram of the area-difference-elasticity model and shape calculations within this model can be used to obtain results for the two-component system. As an illustrative example, consider the thermal evolution of an initially spherical vesicle (with a homogeneous composition profile $\phi(s) = 0$) with increasing temperature, see fig. 21 taken from ref. [13]. With increasing temperature, the reduced volume decreases and the shape becomes more prolate. The inhomogeneous curvature then induces a non-trivial composition profile along the contour. In the outer monolayer, the A molecules are enriched at the poles (if their enhancement in the outer layer leads to a positive spontaneous curvature, i.e. if $\lambda > 0$) while the B lipids are enriched along the equatorial region of the vesicle. For smaller v, the up/down asymmetric shapes have lower energy leading to a discontinuous budding transition. These shapes finally end up at the vesiculation point. In the vesiculated state, the composition within each sphere

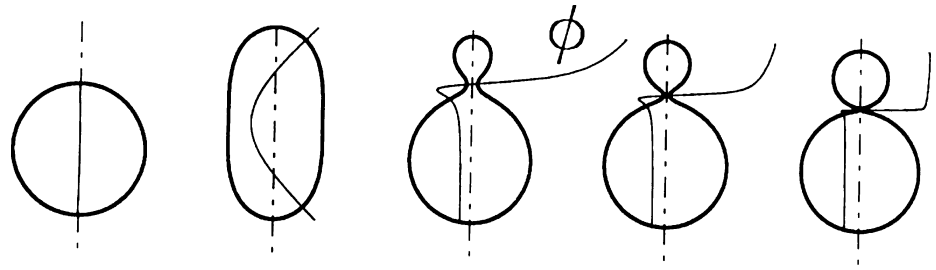

Fig. 21. Curvature-induced lateral phase segregation. The spherical vesicle changes its shape as the reduced volume v decreases due to an increase in temperature. The thin curves show the composition ϕ. The reduced volume is given by $v = 1.0, 0.89, 0.89, 0.86$, and 0.82 from left to right. At $v = 0.89$, the symmetric and the asymmetric shape have the same energy, indicating a discontinuous budding transition. The vesiculation line is reached with the last shape [13].

becomes homogeneous again with all the variation of the composition occurring in the neck. Thus, the shape change, i.e. in this case budding and vesiculation, leads to phase segregation.

6.3.3. Magnitude of curvature-induced phase segregation

A crude estimate for the magnitude of the curvature-induced phase segregation can be obtained as follows [13]. As explained above, a typical value for the coupling λ might be $\lambda \simeq 0.1/$ nm. For the free energy density coefficient ε, one estimates $\varepsilon \simeq \tau T/\kappa a^2$ where a is a molecular length $a \simeq 1$ nm. The reduced temperature $\tau \equiv (T - T_{\rm C})/T_{\rm C}$ is the distance to the A-B critical point which separates the one-phase region from the two-phase coexistence region of the lipid mixture. For a mixture of DEPC and DPPE, this critical point is at $T_{\rm c} \simeq 340K$ according to ref. [111]. For a vesicle at a temperature of 10 centigrades above $T_{\rm c}$, $\tau \simeq 0.03$ which leads with $T/\kappa \simeq 1/25$ to $\phi \simeq 20(H - \Delta A/(4dA))$ nm. With $(H - \Delta A/(4dA_0)) \simeq 1/R_0$, where R_0 is the radius of the vesicle, the typical variation in the composition becomes of the order of 1% for vesicles with a radius $R_0 \simeq 1$ μm but 10% for $R_0 \simeq$ 100 nm. The smaller the vesicles are the larger becomes the phase segregation.

Very close to the critical point, the argument given above that the correlation length is small compared with the size of the vesicle is no longer valid. In fact, using $\xi \simeq a/\tau^{\nu}$, where $a \simeq 1$ nm and $\nu = 1$ is the critical exponent of the two-dimensional Ising model, one obtains $\tau_* \simeq a/R$ as a crossover temperature. For $\tau \lesssim \tau_*$, the gradient term in F_2 can no longer be neglected.

7. Adhesion

7.1. Contact potential and contact curvature

A vesicle near a wall or substrate experiences various forces, such as electrostatic, Van der Waals and hydration forces. The typical range of these forces is several nanometers which is small compared to the size of a large vesicle which is of the order of several microns. Thus, in a first step, the microscopic interaction potential

may be replaced by a contact potential with strength W if we are mainly interested in the gross features of such a vesicle bound to the wall [20].

There are several experimental methods by which one can infer information about the effective interaction $V_{\rm eff}(l)$ between two membranes or between a membrane and another surface which are separated by a thin liquid film of thickness l. These methods include X-ray diffraction on oriented multilayers [124], the surface force apparatus [125], micropipet aspiration [126], and video microscopy of dilute systems [127]. The contact potential W is then identified with $V_{\rm eff}(l_0)$ where l_0 is the mean separation of the membrane in the absence of an external pressure, see chapter 11 in this volume. The value of $W \simeq V_{\rm eff}(l_0)$ depends on the strength of the shape fluctuations which can be reduced by lateral tension or by immobilizing the membranes on solid surfaces. Therefore, the different experimental methods give, in general, different values for W which are in the range between 10^{-4}–1 mJ/m^2. For rough estimates in this section, we will use the value of 1 mJ/m^2 for *strong* adhesion, and the value of 10^{-4} mJ/m^2 for *weak* adhesion.

If the vesicle and the wall have the contact area A^*, the vesicle gains the adhesion energy

$$F_{\rm a} = -WA^* \tag{55}$$

which must be added to the curvature energy. The balance between the gain in adhesion energy and the cost in curvature energy for a bound vesicle gives rise to several interesting phenomena [20]. A first manifestation of this balance is a condition for the contact curvature $1/R_1^*$ which is determined by [20]

$$1/R_1^* = (2W/\kappa)^{1/2}. \tag{56}$$

The contact angle is necessarily π since any sharp bent would have an infinite curvature energy. This implies that the membrane is only curved in one direction and $1/R_2^* = 0$ along the line of contact. Therefore, the same boundary condition (56) also holds for a cylindrical geometry for which it also applies to polymerized membranes or solid-like sheets [128].

The universal condition (56) for the contact curvature holds irrespective of the size of the vesicle and the non-local energy contribution. Thus, a measurement of $1/R_1^*$ yields a value of the contact potential once the bending rigidity κ is known. The range of contact curvatures to be expected from this relation spans $1/R_1^* \simeq 1/10$ nm for strong adhesion (using $\kappa = 10^{-19}$ J) and $1/R_1^* \simeq 1\ \mu$m^{-1} for weak adhesion. The latter value clearly is accessible by light microscopy. In fact, a measurement of the contact curvature has recently been performed using reflection interference contrast microscopy [24].

7.2. Adhesion transition

7.2.1. Bound shapes

Solving the shape equations for axisymmetric shapes with the boundary condition (56) leads to a variety of bound shapes which can be arranged in a phase diagram

as in the case of free vesicles. The basic physics behind the competition between adhesion and curvature energy becomes already evident in the simplest non-trivial ensemble, which contains only the local bending energy with $C_0 = 0$, the adhesion energy and a constraint on the total area. This corresponds to a situation where the volume can adjust freely. With decreasing strength of the contact potential W, the area of contact A^* also decreases and vanishes for $W = W_{\rm a}$, with

$$W_{\rm a} = 2\kappa/R^2. \tag{57}$$

At this value, the bound shape resembles the free shape corresponding to the same constraint which is a sphere except for the fact that the contact curvature $1/R_1^* = 2/R$ is *twice* the curvature of the sphere. However, the contact *mean* curvature $H^* \equiv (1/R_1^* + 1/R_2^*)/2 = 1/R$ is equal to the mean curvature of the sphere. For $W < W_{\rm a}$, an attractive potential does not lead to a bound shape with finite area of contact. Thus, the vesicle undergoes a continuous adhesion transition at $W = W_{\rm a}$ [20].

A somewhat more complex situation arises when, in addition, the enclosed volume is also kept constant. The phase diagram becomes two-dimensional and depends on v and the reduced potential strength

$$w \equiv WR^2/\kappa. \tag{58}$$

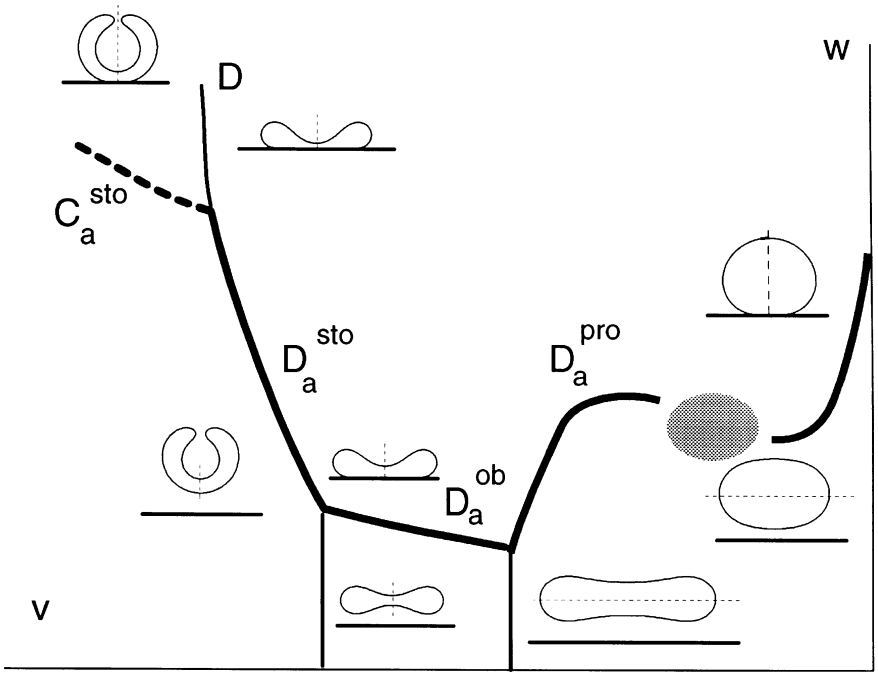

Fig. 22. Schematic phase diagram with free and bound shapes at constant area and volume. The heavy lines show the adhesion transition at $W = W_{\rm a}$, which can be discontinuous ($D_{\rm a}^{\rm pro}$, $D_{\rm a}^{\rm ob}$ and $D_{\rm a}^{\rm sto}$) or continuous ($C_{\rm a}^{\rm sto}$). In the dashed region, non-axisymmetric bound shapes are relevant. The dashed straight lines across the shapes denotes the axis of symmetry [21].

This phase diagram is shown in fig. 22 together with some bound shapes [21, 129, 130]. Its main characteristic is the line of adhesion transitions $w_a(v)$ which separates bound from free states.

The four-dimensional phase diagram for adhesion including the full area-difference-elasticity energy has not yet been studied. In analogy to the free case, one expects that the non-local energy favours continuous adhesion transitions and the occurrence of non-axisymmetric shapes.

7.2.2. Possible experimental verification

Two very different approaches are conceivable in order to observe the adhesion transition experimentally. (i) Changing the temperature will affect both the reduced volume and the scaled adhesion potential $w = WR^2/\kappa$ via the area expansion. A temperature decrease also decreases w and increases v. Therefore, a bound vesicle may become free upon cooling provided its initial state at the higher temperature is already sufficiently close to the adhesion transition. Likewise, osmotic deflation or inflation which does not affect w can induce a crossing of the adhesion transition in the phase diagram. (ii) A more indirect but quite elegant confirmation of the theory described above could make use of the characteristic size-dependence of the adhesion transition as expressed in eq. (57). This relation implies that, for fixed W, in an ensemble of vesicles only those vesicles with $R > R_a \equiv (2\kappa/W_a)^{1/2}$ are bound to the substrate.

7.2.3. Non-axisymmetric shapes

For adhesion, non-axisymmetric shapes are more relevant than in the case of free vesicles, since the axisymmetry of free prolates is broken if these shapes adhere with their long axis parallel to the substrate. Such a bound shape can no longer be obtained by solving the axisymmetric shape equations. However, some insight into the relevance of non-axisymmetric bound shapes can be obtained as follows [21]. The critical value W_a for the *continuous* adhesion transition for the stomatocytes and the oblates (not appearing in the phase diagram) obeys the condition that for small A^*, the contact mean curvature of the bound shape, $H^* \equiv (1/R_1^* + 1/R_2^*)/2 = 1/2R_1^*$, becomes identical to the mean curvature H_f of the corresponding free shape at the point of contact. Using (57) this condition locates the *continuous* adhesion transition at

$$W_a = 2\kappa H_f^2. \tag{59}$$

For a sphere, one has $H_f = 1/R$ and one recovers the relation (57).

If the condition (59) is also valid for a (hypothetical) continuous transition of the prolates and dumbbells (with their axis of symmetry parallel to the wall), one finds that non-axisymmetric bound prolates show up as lowest energy states in the phase diagram, as indicated in fig. 22. It remains to be seen whether the adhesion transition to these states is continuous at $W_a = 2\kappa H_f^2$ (where H_f is the mean curvature at the equator of the prolate) or discontinuous at $W_a < 2\kappa H_f^2$ and how far this region of non-axisymmetric bound shapes extends in the phase diagram. With increasing W, these non-axisymmetric states should then undergo a transition to axisymmetric bound shapes.

7.2.4. Beyond the contact potential

Further insight into the character of the adhesion transition arises from two ramifications of the simple picture presented so far. First, consider the influence of the small but finite range of the potential [131, 132]. We assume that the potential can be characterized by a depth W and a range Z_0. It turns out that the free state discussed above for $W < W_a$, corresponds for such a potential to a pinned state where the vesicle adheres to the wall but keeps its free shape [21, 132]. The energy gain associated with such a pinned state is

$$\Delta F \sim -WRZ_0, \tag{60}$$

for small Z_0/R. Second, we have to compare this energy with the thermal energy $\sim T$ to decide whether it is sufficient to pin the vesicle to the substrate. This comparison leads to a transition between the pinned state and the free state at

$$W_p \sim T/(RZ_0) \quad \text{for} \quad Z_0 \ll R \lesssim R_c \equiv (\kappa/T)Z_0. \tag{61}$$

The length scale R_c arises from the consistency requirement that $W < W_a$, which was assumed when using the estimate (60) for ΔF. The breakdown of this relation for $R > R_c$ indicates that large vesicles will not enter the pinned regime because the energy gain ΔF of such a pinned state would be smaller than the thermal energy T. These large vesicles unbind at values of the potential depth W for which the analysis at $T = 0$ predicts bound vesicles with a finite contact area. The critical strength for the unbinding of these large vesicles is bounded above by the critical strength

$$W_u \sim T^2/(\kappa Z_0^2), \tag{62}$$

for the unbinding of open almost planar membranes [133, 134]. If the enclosed volume does not change during the adhesion process, an effective tension builds up which will decrease the value of the critical strength for unbinding. A refined theory of the unbinding of large vesicles which takes into account the fluctuations in the presence of constraints has yet to be worked out. The estimates given in this section for the adhesion transition of vesicles lead to three different regimes as shown and described in fig. 23 taken from ref. [21].

The crossover length R_c which separates the two qualitatively different regimes of unbinding can be estimated as follows. With the typical values $Z_0 = 4$ nm and $\kappa/T = 25$, we find $R_c = 0.1$ μm which is just below optical resolution. It might, however, be shifted to larger values using multi-lamellar vesicles because κ is proportional to the number of bilayers.

7.3. Effective contact angle for strong adhesion

The adhesion transition takes place for $R = R_a = (w_a\kappa/W)^{1/2}$, where w_a is a numerical coefficient of O(1) which depends on the constraints. For large vesicles with $R \gg R_a$, i.e. for strong adhesion $W \gg W_a$, the shape of the bound vesicle

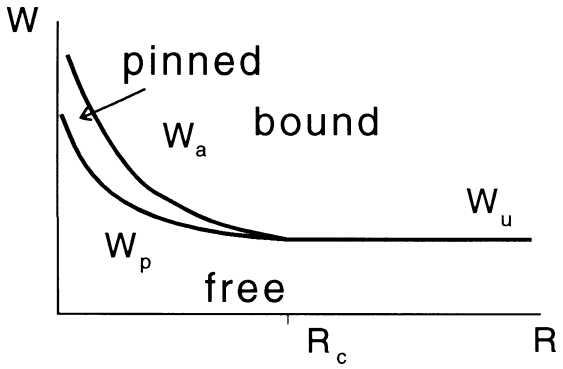

Fig. 23. Schematic phase diagram for adhesion in a potential with finite range $Z_0 \ll R$ and strength W at finite temperature T. Depending on the length scales R and R_c, two different regimes must be distinguished for the unbinding: Small vesicles with $R < R_c$ first undergo the curvature driven transition from a bound state with finite contact area to the pinned state with the nearly free shape for $W \simeq W_a$. These small vesicles then unbind via thermal activation at $W \simeq W_p$. Large vesicles with $R > R_c$, cannot enter the regime of pinned states since they unbind via shape fluctuations in the contact zone at $W \simeq W_u$ [21].

approaches a simple limit shape. If only the area is constrained, this limit shape is a pancake with an energy

$$F \approx -2\pi W R^2 + 2\pi g(2\kappa W)^{1/2} R \tag{63}$$

with the dimensionless coefficient $g \simeq 2.8$ [129]. If in addition the volume is constrained, the vesicle becomes a spherical cap for strong adhesion as shown in fig. 24. In both cases, an *effective contact angle* Ψ_{eff} can be defined which obeys a Young–Dupré equation [20]

$$W = \Sigma(1 + \cos\Psi_{\text{eff}}). \tag{64}$$

For the pancake, one has $\Psi_{\text{eff}} = 0$.

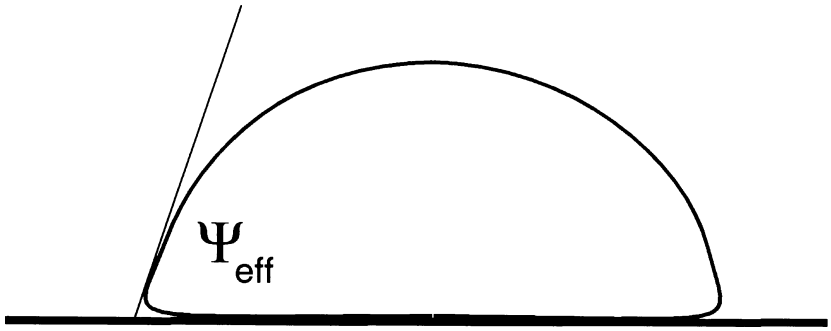

Fig. 24. Bound shape for strong adhesion with effective contact angle Ψ_{eff}. The shape resembles a spherical cap except close to the line of contact [20].

The quantity Σ in (64) is the (numerical) value of the Lagrange multiplier for the area constraint. It also obeys the relation $\Sigma = \partial F/\partial A$ at constant V. Although it is tempting to identify Σ with a lateral tension, this is not justified a priori since we are dealing so far with an incompressible membrane of fixed area. However, it can be shown for free vesicles as well as for bound vesicles, that the strength of most of the fluctuations around a mean shape does not depend on whether a constraint on area and enclosed volume is imposed or whether the energy terms ΣA and PV are added to the bending energy [135].

For strong adhesion, the energetic competition which determines the conformation does not involve the balance between curvature energy and the adhesion energy but rather the balance between the adhesion energy and an elastic stretching of the membrane. This elastic energy reads

$$F_k \equiv (k/2)(A - A_0)^2/A_0 \tag{65}$$

where k is the area compressibility modulus of the order of 10^2 mJ/m^2. Such an extended model leads to the same shape equations as the model with a hard area constraint. Even the boundary condition (56) remains unchanged. The phase diagram, however, changes due to the additional energy. Balancing the adhesion energy with the stretching term leads to the adhesion-induced stretching of the order of

$$(A - A_0)/A_0 \simeq W/k. \tag{66}$$

The relative area expansion $(A - A_0)/A_0$ thus becomes 0.01 for strong adhesion. Identifying $k(A - A_0)/A_0$ with an elastic tension $\Sigma_{\rm el}$, we find the relation $\Sigma_{\rm el} \sim W$ for strong adhesion. As soon as W exceeds the lysis tension which is of the order of 1–5 mJ/m^2, the bound vesicle ruptures.

7.4. Adhesion-induced fusion and rupture

So far, an isolated vesicle at a wall has been considered. If more and more bound vesicles cover the wall, they will come into contact and may fuse. For free vesicles, fusion of two vesicles with equal area $A \equiv 4\pi R^2$ (but no constraint on the volume) leads to a gain in energy $\Delta F_{\rm fv} = 8\pi\kappa + 4\pi\kappa_{\rm G}$. If two bound vesicles fuse, the gain in energy is always larger and satisfies $\Delta F_{\rm bv} \geqslant \tilde{g}\pi\kappa + 4\pi\kappa_{\rm G}$ with $\tilde{g} \simeq 8.3$ [129]. For large R, this energy gain behaves as $\Delta F_{\rm bv} \approx 4\pi g(\sqrt{2} - 1)(\kappa W)^{1/2} R$, where (63) has been used. Thus, adhesion favors fusion.

As the size of the fused vesicle increases, its shape becomes more like the shape of a pancake. If the elastic tension exceeds the threshold for lysis, the pancake ruptures and becomes an open bound disc. The threshold for lysis typically occurs for $(A - A_0)/A_0 \simeq 0.03$. From (66) one then derives that the adhesion potential has to be stronger than $0.03k$ for adhesion induced rupture to happen. Note, however that this argument provides only an upper limit on the adhesion energy required for rupture since it neglects the fact that in the pancake conformation rupture may happen more easily along the strongly curved rim.

After the bound vesicle has ruptured, its conformation becomes an open disc. Such a bound disc has an energy [129]

$$F_{\rm bd} = -4\pi W R^2 + 4\pi \Sigma_{\rm e} R, \tag{67}$$

where $\Sigma_{\rm e}$ is the edge tension along the circumference of the bound disk. A comparison of the energy (67) with the energy (63) of a pancake shows that for $R \gg R_{\rm bd} \equiv \Sigma_{\rm e}/W$ the bound disc always has lower energy (irrespective of the value of the other parameters). For phospholipid bilayers, we find with the typical value $\Sigma_{\rm e} = 5 \times 10^{-20}$ J/nm the length scale $R_{\rm bd} = 50$ nm for strong adhesion and $R_{\rm bd} = 500$ μm for weak adhesion.

A recent experiment has shown that a lamellar structure can form at the air-water interface of a vesicle suspension [136]. The energetic considerations discussed above immediately lead to a scenario where vesicles adhere to the wall, fuse at the wall and rupture. Finally, the open discs will also fuse, thus forming a bilayer parallel to the wall. The same experiment has also revealed that the activation barriers involved in these processes depend sensitively on temperature.

8. Non-fluid membranes: the red blood cell

In this article, we have focused on lipid bilayers in their fluid state. The fluidity allows a simple description of the membranes in terms of two-dimensional surfaces governed by bending elasticity.

Biomembranes always contain a lipid bilayer which is believed to be fluid but, in addition, these membranes also contain attached polymer networks. One example is provided by the plasma membrane of red blood cells which has stimulated much of the early research on membranes but still presents many open problems. We close this article by pointing out the differences between the red blood cell and the artificial vesicles described so far. These remarks are included here in order to emphasize that there remain significant challenges for our understanding of biological membranes in spite of the progress which we have recently made for lipid bilayers.

The plasma membrane of the red-blood-cell has a rather complex architecture [1]. Apart from the lipid bilayer, it contains a network of spectrin tetramers linked together at junctional complexes which forms a quasi-hexagonal structure. The spectrin network and its junctional complexes are attached to the bilayer by integral membrane proteins. The average mesh size of the spectrin network is 70 nm while the maximal extension of a spectrin tetramer is 200 nm.

The spectrin network can be isolated by dissolving the lipid with detergents. The spectrin net then no longer has the typical biconcave shape of the red blood cell but rather becomes nearly spherical. Its morphological and elastic properties can be studied if the skeletons are suspended with optical tweezers in a flow chamber [137]. Likewise, X-ray diffraction as well as light scattering [138] probe the structural properties of this network which can then be compared with theoretical work on 'solid' or 'tethered' membranes [139, 140].

These two-dimensional membranes have similar elastic properties as bilayer membranes in their gel state or bilayers composed of polymerized lipids. Due to the fixed connectivity within the membranes, these systems can sustain shear deformations. Moreover, since bending typically involves stretching and shearing of the membrane, the in-plane displacements, i.e. phonons, are coupled to the bending modes [128]. This coupling leads to an increase of the effective bending rigidity for long-wavelength bending modes. Solid or polymerized membranes are thus stiffer than fluid ones as can be seen in the microscope: if vesicles are cooled below the chain-melting transition, their flickering is substantially reduced.

For the compound red blood cell membrane, the presence of the network poses a conceptual problem for the calculation of shapes since it is not yet clear to which extent the network contributes to the stability of the shape. In fact, we have seen even for lipid vesicles that a discocyte shape minimizes the curvature energy in an appropriate range of the reduced volume. Thus, in the absence of external contact forces, the shape of the red blood cell could be primarily controlled by the osmotic conditions while the cytosceleton is used to recover this shape after deformations of the cell shape. On the other hand, it is known that dissolving the network from the bilayer results in spontaneous budding of small vesicles. Thus, it seems that the network is relevant in stabilizing the red blood cell lipid membrane with its specific composition [141].

Evidence for a presumably subtle interplay between network and bilayer also arises from measurements of the elastic properties of the red blood cell membrane and, in particular, from its shear modulus which seems to be strongly scale-dependent. On large scales, deformation in the micropipet [142] as well as deformation induced by an electric field [143] yield a shear modulus $\mu \simeq 6 \times 10^{-3}$ mJ/m^2. In the analysis of the thickness fluctuations by flicker spectroscopy, which probe smaller scales, however, the resistance to shear is with $\mu \simeq 3 \times 10^{-4}$ mJ/m^2 more than one order of magnitudes smaller [144]. An attractive hypothesis to explain these findings assumes that for small deformations the spectrin remains 'bound' to the bilayer whereas the crosslinks and the anchoring break up or reorganize dynamically when large deformations are applied for a sufficiently long time as in the micropipet experiment [145].

In general, the flickering of a compound membrane such as the plasma membrane of red blood cells should exhibit a crossover scale L_* [146, 147]. For wavelengths $L < L_*$, the shape fluctuations are fluid-like whereas the finite shear modulus of the network only affects the fluctuations of wavelengths $L > L_*$. The crossover length has been estimated both from the nonlinear elastic terms for almost planar membranes [146] and from the linear theory of closed vesicles [147]. In the latter case, one obtains $L_* \simeq R^2\kappa/Y$ where R denotes the radius of curvature of the rest shape and the parameter $Y \simeq 4\mu$ denotes the Young modulus. Using the latest estimates of μ, this leads to $L_* \simeq 0.1$–0.2 μm which is somewhat larger than the meshsize of the network. This estimate is consistent with the naive expectation that the shape fluctuations of the red blood cell are governed by the bending rigidity below this meshsize.

A comprehensive theoretical model for the red blood cell membrane has not yet emerged. Steps in such a direction are provided by a continuum theory in which the

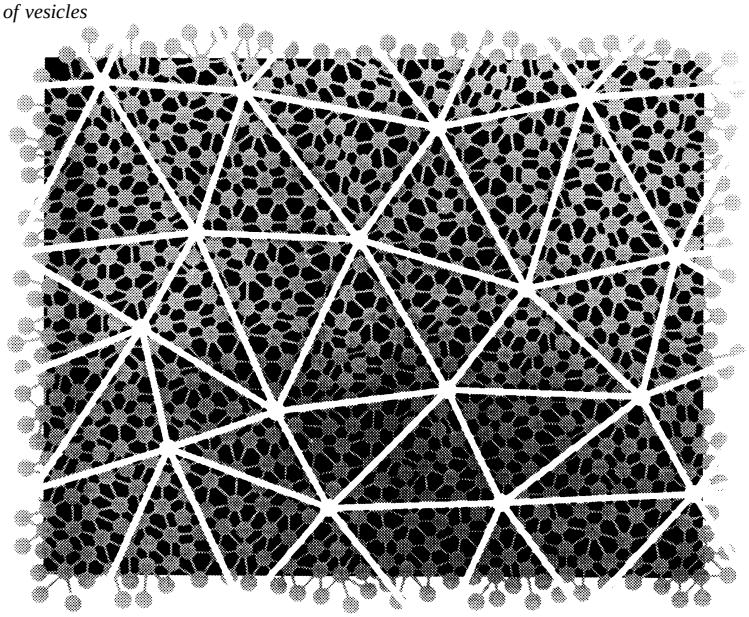

Fig. 25. Dual network model for red blood cell membrane. The grey tethers and beads represent the fluid membrane. Their connectivity is changing dynamically. The white tethers represent spectrin bonds whose connectivity is fixed [150].

network is modeled as an ionic gel [148, 149] as well as by recent computer simulations. As an example of the latter method, fig. 25 shows a dual model in which the lipid bilayer as well as the spectrin net are treated at the same time [150]. The analysis has shown a sensitive dependence of the shear modulus on the maximal extension of the spectrin tethers which was one of the model parameters. Recently, a more refined modelling of the spectrin as a polymer chain attached to the bilayer led to reasonable agreement with experimental data [151]. Whether computer simulations of more sophisticated membrane structures, more advanced elasticity continuum theories or a combination of both will finally be most useful in order to understand the red blood cell membrane remains to be seen.

A. Derivation of the area-difference-elasticity model

The area-difference-elasticity energy can be derived by first introducing two densities $\phi^{\pm}$ for the two monolayers. Since we want to keep a single surface for the description of the vesicle shape, we have to define the densities relative to this surface which is the neutral surface of the bilayer. The elasticity, however, acts in the neutral surface of each of the two monolayers, see fig. 26. The densities $\phi^{\pm}$ within these neutral surfaces can be projected onto the neutral surface of the bilayer. The value of these projected densities $\phi^{\pm}_{\mathrm{proj}}$ depends on the local mean curvature of the bilayer neutral surface through

$$\phi^{\pm} \approx \phi^{\pm}_{\mathrm{proj}}(1 \mp 2dH) \tag{68}$$

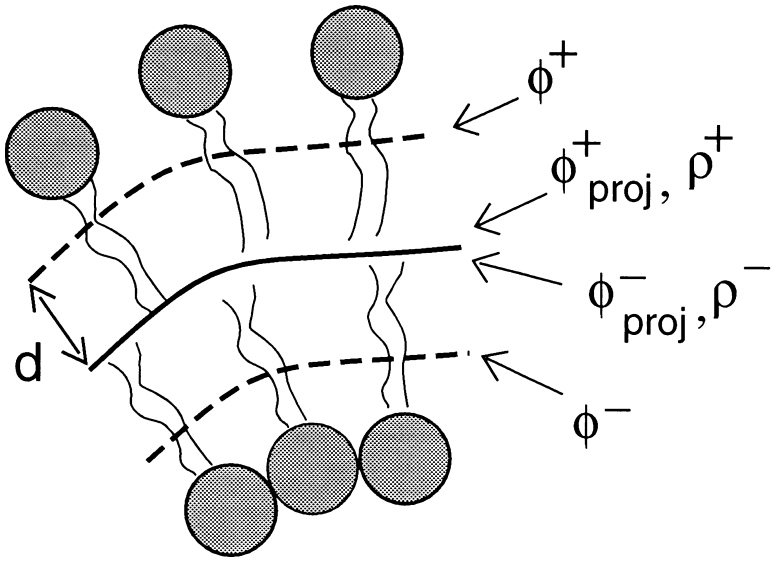

Fig. 26. Schematic geometry of a bilayer membrane. The circles with tails represent the lipid molecules. The dashed lines are the neutral surfaces of the monolayers, on which the densities $\phi^{\pm}$ are defined. The dark solid line is the midsurface of the bilayer, on which the projected densities $\phi^{\pm}_{\text{proj}}$ and the scaled projected densities $\rho^{\pm}$ are defined.

with the convention that H is positive for a sphere.

Consequently, the local elastic energy density of each monolayer reads

$$\left(k^{(m)}/2\right)\left(\phi^{\pm}/\phi_0 - 1\right)^2 \approx \left(k^{(m)}/2\right)\left(\rho^{\pm} \mp 2dH\right)^2$$

where $\rho^{\pm} \equiv (\phi^{\pm}_{\text{proj}}/\phi_0 - 1)$ is the scaled deviation of the projected density from its equilibrium value ϕ_0 for a flat membrane. Here, $k^{(m)}$ is the compression modulus for the monolayers. Adding these energies to the local bending energy (3), one ends up with the local energy [88]

$$f = \frac{\kappa}{2}(2H)^2 + \frac{k^{(m)}}{2}\left[\left(\rho^+ - 2dH\right)^2 + \left(\rho^- + 2dH\right)^2\right], \tag{69}$$

where we assume for simplicity a symmetric bilayer. The coupling between the monolayers densities and the shape becomes evident if the the average density (deviation) $\bar{\rho} \equiv (\rho^+ + \rho^-)/2$ and the density difference (deviation) $\rho \equiv (\rho^+ - \rho^-)/2$ are introduced in (69). This leads to the local energy

$$f = \frac{\kappa}{2}(2H)^2 + k^{(m)}\left[\bar{\rho}^2 + (\rho - 2dH)^2\right]. \tag{70}$$

Since the average density $\bar{\rho}$ does not couple to the shape, a homogeneous distribution with the average value of the density given by the equilibrium value ϕ_0, i.e.

$\bar{\rho} = 0$, minimizes this elastic energy, thus determining the area of the vesicle through the total number of molecules, as in section 2.2. The density difference, $\rho(s_1, s_2)$, however, becomes inhomogeneous because it adapts locally to the shape through

$$\rho(s_1, s_2) = 2d\big[H(s_1, s_2) - M/A\big] + \big(N^+ - N^-\big)/(2\phi_0 A). \tag{71}$$

This relation can be derived by introducing a Lagrange multiplier for the constraint

$$\oint \mathrm{d}A\rho = \big(N^+ - N^-\big)/(2\phi_0),$$

where N^+ and N^- are the number of molecules in the outer and inner monolayer, respectively, and then minimizing (70) with respect to $\rho(s_1, s_2)$. The geometrical quantity $M \equiv \oint \mathrm{d}A\ H$ denotes the total mean curvature. Insertion of this density distribution into (70) and integrating over the vesicle surface leads to the energy (11) given in section 2.3 if the elastic term for the total area is omitted.

References

1. Alberts, B., D. Bray, J. Lewis, M. Raff, K. Roberts and J.D. Watson, 1989, Molecular Biology of the Cell, 2nd edition (Garland, New York).
2. Canham, P.B., 1970, The minimum energy of bending as a possible explanation of the biconcave shape of the human red blood cell, J. Theoret. Biol. **26**, 61–81.
3. Helfrich, W., 1973, Elastic properties of lipid bilayers: Theory and possible experiments, Z. Naturforsch. **28c**, 693–703.
4. Deuling H.J. and W. Helfrich, 1976, The curvature elasticity of fluid membranes: A catalogue of vesicle shapes, J. Physique **37**, 1335–1345.
5. Evans, E.A., 1974, Bending resistance and chemically induced moments in membrane bilayers, Biophys. J. **14**, 923–931.
6. Svetina, S. and B. Zeks, 1989, Membrane bending energy and shape determination of phospholipid vesicles and red blood cells, Eur. Biophys. J. **17**, 101–111.
7. Berndl, K., J. Käs, R. Lipowsky, E. Sackmann and U. Seifert, 1990, Shape transformations of giant vesicles: Extreme sensitivity to bilayer asymmetry, Europhys. Lett. **13**, 659–664.
8. Miao, L., B. Fourcade, M. Rao, M. Wortis and R.K.P. Zia, 1991, Equilibrium budding and vesiculation in the curvature model of fluid lipid vesicles, Phys. Rev. A **43**, 6843–6856.
9. Seifert, U., K. Berndl and R. Lipowsky, 1991, Shape transformations of vesicles: Phase diagrams for spontaneous-curvature and bilayer-coupling models, Phys. Rev. A **44**, 1182–1202.
10. Sackmann, E., H.-P. Duwe and H. Engelhardt, 1986, Membrane bending elasticity and its role for shape fluctuations and shape transformations of cells and vesicles, Faraday Discuss. Chem. Soc. **81**, 281–290.
11. Käs, J. and E. Sackmann, 1991, Shape transitions and shape stability of giant phospholipid vesicles in pure water induced by area-to-volume changes, Biophys. J. **60**, 825–844.
12. Lipowsky, R., 1992, Budding of membranes induced by intramembrane domains, J. Phys. II France **2**, 1825–1840.
13. Seifert, U., 1993, Curvature-induced lateral phase segregation in two-component vesicles, Phys. Rev. Lett. **70**, 1335–1338.
14. Döbereiner, H.-G., J. Käs, D. Noppl, I. Sprenger and E. Sackmann, 1993, Budding and fission of vesicles, Biophys. J. **65**, 1396–1403.
15. Seifert, U., 1991, Vesicles of toroidal topology, Phys. Rev. Lett. **66**, 2404–2407.
16. Jülicher, F., U. Seifert and R. Lipowsky, 1993, Phase diagrams and shape transformations of toroidal vesicles, J. Phys. II France **3**, 1681–1705.

17. Jülicher, F., U. Seifert and R. Lipowsky, 1993, Conformal degeneracy and conformal diffusion of vesicles, Phys. Rev. Lett. **71**, 452–455.
18. Fourcade, B., M. Mutz and D. Bensimon, 1992, Experimental and theoretical study of toroidal vesicles, Phys. Rev. Lett. **68**, 2551–2554.
19. Michalet, X., 1994, Etude expérimentale de vésicule phospholipidiques de genre topologique non sphérique, PhD thesis, l'Université de Paris VII.
20. Seifert U. and R. Lipowsky, 1990, Adhesion of vesicles, Phys. Rev. A **42**, 4768–4771.
21. Seifert, U. and R. Lipowsky, 1991, Adhesion and unbinding of vesicles, in: Dynamical Phenomena at Interfaces, Surfaces and Membranes, eds D. Beysens, N. Boccara and G. Forgacz (Nova Science, New York) pp. 295–304.
22. Evans, E.A., 1980, Analysis of adhesion of large vesicles to surfaces, Biophys. J. **31**, 425–432.
23. Zilker, A., H. Engelhardt and E. Sackmann, 1987, Dynamic reflection interference contrast (RIC-) microscopy: A new method to study surface excitations of cells and to measure membrane bending elastic moduli, J. Physique **48**, 2139–2151.
24. Rädler, J. and E. Sackmann, 1993, Imaging optical thicknesses and separation distances of phospholipid vesicles at solid surfaces, J. Phys. II France **3**, 727–748.
25. Sackmann, E., 1990, Molecular and global structure and dynamics of membranes and lipid bilayers, Can. J. Phys. **68**, 999–1012.
26. Lipowsky, R., 1991, The conformation of membranes, Nature **349**, 475–481.
27. Wortis, M., U. Seifert, K. Berndl, B. Fourcade, L. Miao, M. Rao and R.K.P. Zia, 1991, Curvature-controlled shapes of lipid-bilayer vesicles: Budding, vesiculation and other phase transitions, in: Dynamical Phenomena at Interfaces, Surfaces and Membranes, eds D. Beysens, N. Boccara and G. Forgacs (Nova Science, New York) pp. 221–236.
28. Backer, J.M. and E.A. Dawidowicz, 1981, Transmembrane movement of cholesterol in small unilamellar vesicles detected by cholesterol oxidase, J. Biol. Chem. **256**, 586–588.
29. Fischer, T.M., 1993, Bending stiffness of lipid bilayers, V. Comparison of two formulations, J. Phys. II France **3**, 1795–1805.
30. Helfrich, W., 1974, Blocked lipid exchanges in bilayers and its possible influence on the shape of vesicles, Z. Naturforsch. **29c**, 510–515.
31. Seifert, U., L. Miao, H.-G. Döbereiner and M. Wortis, 1991, Budding transition for bilayer fluid vesicles with area-difference elasticity, in: The Structure and Conformation of Amphiphilic Membranes. Springer Proceedings in Physics, Vol. 66, eds R. Lipowsky, D. Richter and K. Kremer (Springer, Berlin) pp. 93–96.
32. Wiese, W., W. Harbich and W. Helfrich, 1992, Budding of lipid bilayer vesicles and flat membranes, J. Phys. Condens. Matter **4**, 1647–1657.
33. Bozic, B., S. Svetina, B. Zeks and R.E. Waugh, 1992, Role of lamellar membrane structure in tether formation from bilayer vesicles, Biophys. J. **61**, 963–973.
34. Evans, E.A., 1980, Minimum energy analysis of membrane deformation applied to pipet aspiration and surface adhesion of red blood cells, Biophys. J. **30**, 265–284.
35. Sheetz, M.P. and S.J. Singer, 1974, Biological membranes as bilayer couples. A molecular mechanism of drug-erythrocyte interactions, Proc. Nat. Acad. Sci. USA **71**, 4457–4461.
36. Svetina, S. and B. Zeks, 1992, The elastic deformability of closed multilayered membranes is the same as that of a bilayer membrane, Eur. Biophys. J. **21**, 251–255.
37. Svetina, S., M. Brumen and B. Zeks, 1985, Lipid bilayer elasticity and the bilayer couple interpretation of red cell shape transformations and lysis, Stud. Biophys. **110**, 177–184.
38. Miao, L., 1992, Equilibrium shapes and shape transitions of fluid lipid-bilayer vesicles, PhD thesis, Simon Fraser University.
39. Miao, L., U. Seifert, M. Wortis and H.-G. Döbereiner, 1994, Budding transitions of fluid-bilayer vesicles: The effect of area-difference elasticity, Phys. Rev. E, in press.
40. Svetina, S. and B. Zeks, 1983, Bilayer couple hypothesis of red cell shape transformations and osmotic hemolysis, Biochim. Biophys. Acta **42**, 86–90.
41. Evans, E.A., 1983, Bending elastic modulus of red blood cell membrane derived from buckling instability in micropipet aspiration tests, Biophys. J. **43**, 27–30.

42. Evans, E. and D. Needham, 1987, Physical properties of surfactant bilayer membranes: Thermal transitions, elasticity, rigidity, cohesion, and colloidal interactions, J. Phys. Chem. **91**, 4219–4228.
43. Bo, L. and R.E. Waugh, 1989, Determination of bilayer membrane bending stiffness by tether formation from giant, thin-walled vesicles, Biophys. J. **55**, 509–517.
44. Waugh, R.E., J. Song, S. Svetina and B. Zeks, 1992, Local and nonlocal curvature elasticity in bilayer membranes by tether formation from lecithin vesicles, Biophys. J. **61**, 974–982.
45. Schneider, M.B., J.T. Jenkins and W.W. Webb, 1984, Thermal fluctuations of large quasi-spherical bimolecular phospholipid vesicles, J. Phys. **45**, 1457–1472.
46. Engelhardt, H., H.P. Duwe and E. Sackmann, 1985, Bilayer bending elasticity measured by Fourier analysis of thermally excited surface undulations of flaccid vesicles, J. Physique Lett. **46**, L395–L400.
47. Bivas, I., P. Hanusse, P. Bothorel, J. Lalanne and O. Aguerre-Chariol, 1987, An application of the optical microscopy to the determination of the curvature elastic modulus of biological and model membranes, J. Phys. **48**, 855–867.
48. Faucon, J.F., M.D. Mitov, P. Meleard, I. Bivas and P. Bothorel, 1989, Bending elasticity and thermal fluctuations of lipid membranes. Theoretical and experimental requirements, J. Phys. France **50**, 2389–2414.
49. Duwe, H.P., J. Käs and E. Sackmann, 1990, Bending elastic moduli of lipid bilayers: Modulation by solutes, J. Phys. France **51**, 945–962.
50. Meleard, P., J.F. Faucon, M.D. Mitov and P. Bothorel, 1992, Pulsed-light microscopy applied to the measurement of the bending elasticity of giant liposomes, Europhys. Lett. **19**, 267–271.
51. Schneider, M.B., J.T. Jenkins and W.W. Webb, 1984, Thermal fluctuations of large cylindrical phospholipid vesicles, Biophys. J. **45**, 891–899.
52. Mutz, M. and W. Helfrich, 1990, Bending rigidities of some biological model membranes as obtained from the Fourier analysis of contour sections, J. Phys. France **51**, 991–1002.
53. Rädler, J., 1993, Über die Wechselwirkung fluider Phospholipid-Membranen mit Festkörperoberflächen, PhD thesis, TU München.
54. Helfrich, W. and R.-M. Servuss, 1984, Undulations, steric interaction and cohesion of fluid membranes, Il Nuovo Cimento **3D**, 137–151.
55. Evans, E. and W. Rawicz, 1990, Entropy-driven tension and bending elasticity in condensed-fluid membranes, Phys. Rev. Lett. **64**, 2094–2097.
56. Kummrow, M. and W. Helfrich, 1991, Deformation of giant lipid vesicles by electric fields, Phys. Rev. A **44**, 8356–8360.
57. Helfrich, W., 1989, Hats and saddles in liquid membranes, Liq. Cryst. **5**, 1647–1658.
58. Helfrich, W. and B. Klösgen, 1992, Some complexities of simple liquid membranes, in: Dynamical Phenomena at Interfaces, Surfaces and Membranes (Nova Science, New York) pp. 211–220.
59. Song, J. and R.E. Waugh, 1993, Bending rigidity of SOPC membranes containing cholesterol, Biophys. J. **64**, 1967–1970.
60. Jülicher, F. and R. Lipowsky, 1993, Domain-induced budding of vesicles, Phys. Rev. Lett. **70**, 2964–2967.
61. de Gennes, P.G. and C. Taupin, 1982, Microemulsions and the flexibility of oil/water interfaces, J. Phys. Chem. **86**, 2294–2304.
62. Gompper, G. and D.M. Kroll, 1992, Inflated vesicles: A new phase of fluid membranes, Europhys. Lett. **19**, 581–586.
63. Jenkins, J.T., 1977, Static equilibrium configurations of a model red blood cell, J. Math. Biol. **4**, 149–169.
64. Luke, J.C., 1982, A method for the calculation of vesicle shapes, SIAM J. Appl. Math. **42**, 333–345.
65. Peterson, M.A., 1985, An instability of the red blood cell shape, J. Appl. Phys. **57**, 1739–1742.
66. Berndl, K., 1990, Formen von Vesikeln, Diplomarbeit, Ludwig-Maximilians-Universität München.
67. Jülicher, F. and U. Seifert, 1994, Shape equations for axisymmetric vesicles: A clarification, Phys. Rev. E.

68. Heinrich, V., S. Svetina and B. Zeks, 1993, Nonaxisymmetric vesicle shapes in a generalized bilayer-couple model and the transition between oblate and prolate axisymmetric shapes, Phys. Rev. E **48**, 3112–3123.
69. Milner, S.T. and S.A. Safran, 1987, Dynamical fluctuations of droplet microemulsions and vesicles, Phys. Rev. A **36**, 4371–4379.
70. Ou-Yang, Z.-C. and W. Helfrich, 1987, Instability and deformation of a spherical vesicle by pressure, Phys. Rev. Lett. **59**, 2486–2488.
71. Ou-Yang, Z.-C. and W. Helfrich, 1989, Bending energy of vesicle membranes: General expressions for the first, second and third variation of the shape energy and applications to spheres and cylinders, Phys. Rev. A **39**, 5280–5288.
72. Peterson, M.A., 1989, Deformation energy of vesicles at fixed volume and surface area in the spherical limit, Phys. Rev. A **39**, 2643–2645.
73. Heinrich, V., M. Brumen, R. Heinrich, S. Svetina and B. Zeks, 1992, Nearly spherical vesicle shapes calculated by use of spherical harmonics: Axisymmetric and nonaxisymmetric shapes and their stability, J. Phys. II France **2**, 1081–1108.
74. Wiese, W. and W. Helfrich, 1990, Theory of vesicle budding, J. Phys. Condens. Matter **2**, SA329–SA332.
75. Seifert, U., 1990, Shape transformations of free, toroidal and bound vesicles, J. Physique Colloq. **51**, C7339–344.
76. Fourcade, B., L. Miao, M. Rao, M. Wortis and R.K.P. Zia, Scaling Analysis of Narrow Necks in Curvature Models of Fluid Lipid-Bilayer Vesicles, Preprint.
77. Bruinsma, R., 1991, Growth instabilities of vesicles, J. Phys. II France **1**, 995–1012.
78. Käs, J., E. Sackmann, R. Podgornik, S. Svetina and B. Zeks, 1993, Thermally induced budding of phospholipid vesicles – a discontinuous process, J. Phys. II France **3**, 631–645.
79. Nezil, F.A. and M. Bloom, 1992, Combined influence of cholesterol and synthetic amphiphillic peptided upon bilayer thickness in model membranes, Biophys. J. **61**, 1176–1183.
80. Döbereiner, H.-G., Private communication.
81. Farge, E. and P.F. Devaux, 1992, Shape changes of giant liposomes induced by an asymmetric transmembrane distribution of phospholipids, Biophys. J. **61**, 347–357.
82. Boroske, E., M. Elwenspoek and W. Helfrich, 1981, Osmotic shrinkage of giant egg-lecithin vesicles, Biophys. J. **34**, 95–109.
83. Peterson, M.A., 1985, Shape dynamics of nearly spherical membrane bounded fluid cells, Mol. Cryst. Liq. Cryst. **127**, 257–272.
84. Helfrich, W., 1986, Size distributions of vesicles: The role of the effective rigidity of membranes, J. Physique **47**, 321–329.
85. Peterson, M.A., H. Strey and E. Sackmann, 1992, Theoretical and phase contrast microscopic eigenmode analysis of erythrocyte flicker: Amplitudes, J. Phys. II France **2**, 1273–1285.
86. Brochard, F. and J.F. Lennon, 1975, Frequency spectrum of the flicker phenomenon in erythrocytes, J. Physique **36**, 1035–1047.
87. Meleard, P., M.D. Mitov, J.F. Faucon and P. Bothorel, 1990, Dynamics of fluctuating vesicles, Europhys. Lett. **11**, 355–360.
88. Seifert, U. and S.A. Langer, 1993, Viscous modes of fluid bilayer membranes, Europhys. Lett. **23**, 71–76.
89. Evans, E., A. Yeung, R. Waugh and J. Song, 1991, Dynamic coupling and nonlocal curvature elasticity in bilayer membranes, in: The Structure and Conformation of Amphiphilic Membranes. Springer Proceedings in Physics, Vol. 66, eds R. Lipowsky, D. Richter and K. Kremer (Springer, Berlin) pp. 148–153.
90. Fischer, T.M., 1992, Bending stiffness of lipid bilayers, I. Bilayer couple or single-layer bending?, Biophys. J. **63**, 1328–1335.
91. Ou-Yang, Z.-C., 1990, Anchor ring-vesicle membranes, Phys. Rev. A **41**, 4517–4520.
92. Willmore, T.J., 1982, Total Curvature in Riemannian Geometry (Ellis Horwood, Chicester).
93. Duplantier, B., 1990, Exact curvature energies of charged membranes of arbitrary shapes, Physica A **168**, 179–197.
94. Fourcade, B., 1992, Theoretical results of toroidal vesicles, J. Phys. II France **2**, 1705–1724.

95. Seifert, U., 1991, Conformal transformations of vesicle shapes, J. Phys. A: Math. Gen. **24**, L573–L578.
96. Mutz, M. and D. Bensimon, 1991, Observation of toroidal vesicles, Phys. Rev. A **43**, 4525–4527.
97. Kusner, R., 1989, Comparison surfaces for the Willmore problem, Pac. J. Math. **138**, 317–345.
98. Hsu, L., R. Kusner and J. Sullivan, 1992, Minimizing the squared mean curvature integral for surfaces in space forms, Exp. Math. **1**, 191–207.
99. Jülicher, F., 1993, Die Morphologie von Vesikeln, PhD thesis, Universität zu Köln.
100. Karcher, H., U. Pinkall and I. Sterling, 1988, New minimal surfaces in S^3, J. Diff. Geom. **28**, 169–185.
101. Michalet, X., D. Bensimon and B. Fourcade, 1994, Fluctuating vesicles of nonspherical topology, Phys. Rev. Lett. **72**, 168–171.
102. Gruler, H., 1975, Chemoelastic effects of membranes, Z. Naturforsch. **30c**, 608–614.
103. Gebhardt, C., H. Gruler and E. Sackmann, 1977, On domain structure and local curvature in lipid bilayers and biological membranes, Z. Naturforsch. **32c**, 581–596.
104. Lipowsky, R., 1993, Domain-induced budding of fluid membranes, Biophys. J. **64**, 1133–1138.
105. Glaser, M., 1993, Lipid domains in biological membranes, in: Current Opinion in Structural Biology. Current Biology, Vol. 3, pp. 475–481.
106. Leibler, S., 1986, Curvature instability in membranes, J. Physique **47**, 507–516.
107. Leibler, S. and D. Andelman, 1987, Ordered and curved meso-structures in membranes and amphiphilic films, J. Phys. **48**, 2013–2018.
108. Needham, D., T.J. McIntosh and E. Evans, 1988, Thermomechanical and transition properties of dimyristoylphosphatidycholine/cholesterol bilayers, Biochem. **27**, 4668–4673.
109. Vist, M.R. and J.H. Davis, 1990, Phase equilibria of cholesterol/dipalmitoylphosphatidylcholine mixtures: ^{2}H nuclear magnetic resonance and differential scanning calorimetry, Biochemistry **29**, 451–464.
110. Bloom, M., E. Evans and O.G. Mouritsen, 1991, Physical properties of the fluid lipid-bilayer component of cell membranes: A perspective, Q. Rev. Biophys. **24**, 293–397.
111. Wu, S.H.-W. and H.M. McConnell, 1975, Phase separations in phospholipid membranes, Biochemistry **14**, 847–854.
112. Bloom, M., 1992, The physics of soft, natural materials, Phys. Canada **48**(1), 7–16.
113. Andelman, D., T. Kawakatsu and K. Kawasaki, 1992, Equilibrium shape of two-component unilamellar membranes and vesicles, Europhys. Lett. **19**, 57–62.
114. Kawakatsu, T., D. Andelman, K. Kawasaki and K. Taniguchi, 1993, Phase transitions and shape of two component membranes and vesicles, I. Strong segregation limit, J. Phys. II France **3**, 971–997.
115. Kaler, E.W., A.K. Muthy, B.E. Rodriguez and J.A.N. Zasadzinski, 1989, Spontaneous vesicle formation in aqueous mixtures of single-tailed surfactants, Science **245**, 1371–1374.
116. Safran, S.A., P. Pincus and D. Andelman, 1990, Theory of spontaneous vesicle formation in surfactant mixtures, Science **248**, 354–356.
117. Safran, S.A., P.A. Pincus, D. Andelman and F.C. MacKintosh, 1991, Stability and phase behavior of mixed surfactant vesicles, Phys. Rev. A **43**, 1071–1078.
118. Kaler, E.W., K.L. Herrington, A.K. Murthy and J.A.N. Zasadzinski, 1992, Phase behavior and structures of mixtures of anionic and cationic surfactants, J. Phys. Chem. **96**, 6698–6707.
119. MacKintosh, F.C. and T.C. Lubensky, 1991, Orientational order, topology, and vesicle shapes, Phys. Rev. Lett. **67**, 1169–1172.
120. Benvegnu, D.J. and H.M. McConnell, 1992, Line tension between liquid domains in lipid monolayers, J. Phys. Chem. **96**, 6820–6824.
121. Helfrich, W., 1974, The size of bilayer vesicles generated by sonication, Phys. Lett. **50A**, 115–116.
122. Fromherz, P., 1983, Lipid-vesicle structure: Size control by edge-active agents, Chem. Phys. Lett. **94**, 259–266.
123. Boal, D.H. and M. Rao, 1992, Topology changes in fluid membranes, Phys. Rev. A **46**, 3037–3045.
124. Rand, R.P. and V.A. Parsegian, 1989, Hydration forces between phospholipid bilayers, Biochim. Biophys. Acta **988**, 351–376.

125. Marra, J. and J.N. Israelachvili, 1985, Direct measurements of forces between phosphatidylcholine and phosphatidylethanolamine bilayers in aqueous electrolyte solutions, Biochemistry **24**, 4608–4618.
126. Evans, E., 1990, Adhesion of surfactant-membrane covered droplets: Special features and curvature elasticity effects, Coll. Surf. **43**, 327–347.
127. Servuss, R.-M. and W. Helfrich, 1989, Mutual adhesion of lecithin membranes at ultralow tensions, J. Phys. France **50**, 809–827.
128. Landau, L.D. and E.M. Lifshitz, 1989, Elastizitätstheorie (Akademie-Verlag, Berlin).
129. Lipowsky, R. and U. Seifert, 1991, Adhesion of vesicles and membranes, Mol. Cryst. Liq. Cryst. **202**, 17–25.
130. Lipowsky, R. and U. Seifert, 1991, Adhesion of membranes: A theoretical perspective, Langmuir **7**, 1867–1873.
131. Evans, E.A., 1985, Detailed mechanics of membrane-membrane adhesion and separation, I. Continuum of molecular cross-bridges, Biophys. J. **48**, 175–183.
132. Seifert, U., 1991, Adhesion of vesicles in two dimensions, Phys. Rev. A **43**, 6803–6814.
133. Lipowsky, R. and S. Leibler, 1986, Unbinding transitions of interacting membranes, Phys. Rev. Lett. **56**, 2541–2544.
134. Lipowsky, R. and B. Zielinska, 1989, Binding and unbinding of lipid membranes: A Monte Carlo study, Phys. Rev. Lett. **62**, 1572–1575.
135. Seifert, U., Unpublished.
136. Cevc, G., W. Fenzl and L. Sigl, 1990, Surface-induced X-ray reflection visualization of membrane orientation and fusion into multibilayers, Science **249**, 1161–1163.
137. Svoboda, K., C.F. Schmidt, D. Branton and S.M. Block, 1992, Conformation and elasticity of the isolated red blood cell membrane skeleton, Biophys. J. **63**, 784–793.
138. Schmidt, C.F., K. Svoboda, N. Lei, I.B. Petsche, L.E. Berman, C.R. Safinya and G.S. Grest, 1993, Existence of a flat phase in red cell membrane skeletons, Science **259**, 952–955.
139. Nelson, D.R. and L. Peliti, 1987, Fluctuations in membranes with crystalline and hexatic order, J. Phys. France **48**, 1085–1092.
140. Nelson, D., 1988, The statistical mechanics of crumpled membranes, in: Random Fluctuations and Pattern Growth, eds H.E. Stanley and N. Ostrowsky, pp. 193–215.
141. Steck, T.L., 1989, Red cell shape, in: Cell Shape Determinants, Regulation and Regulatory Role, eds W. Stein and F. Bronner (Academic Press, New York) pp. 205–246.
142. Waugh, R. and E.A. Evans, 1979, Thermoelasticity of red blood cell membrane, Biophys. J. **26**, 115–132.
143. Engelhardt, H. and E. Sackmann, 1988, On the measurement of shear elastic moduli and viscosities of erythrocyte plasma membranes by transient deformation in high frequency electric fields, Biophys. J. **54**, 495–508.
144. Strey, H., 1993, Bestimmung Elastischer Eigenschaften von Zellmembranen und Zytoskelett Mittels Flickerspektroskopie, PhD thesis, TU München.
145. Lerche, D., M.M. Kozlov and W. Meier, 1991, Time-dependent elastic extensional RBC deformation by micropipette aspiration: Redistribution of the spectrin network?, Eur. Biophys. J. **19**, 301–309.
146. Lipowsky, R. and M. Girardet, 1990, Shape fluctuations of polymerized or solidlike membranes, Phys. Rev. Lett. **65**, 2893–2896.
147. Komura, S. and R. Lipowsky, 1992, Fluctuations and stability of polymerized vesicles, J. Phys. II France **2**, 1563–1575.
148. Stokke, B.T., A. Mikkelsen and A. Elgsaeter, 1986, The human erythrocyte membrane skeleton may be an ionic gel, I. Membrane mechanochemical properties, Eur. Biophys. J. **13**, 203–218.
149. Stokke, B.T., A. Mikkelsen and A. Elgsaeter, 1986, The human erythrocyte membrane skeleton may be an ionic gel, II. Numerical analyses of cell shapes and shape transformations, Eur. Biophys. J. **13**, 219–233.
150. Boal, D.H., U. Seifert and A. Zilker, 1992, Dual network model for red blood cell membranes, Phys. Rev. Lett. **69**, 3405–3408.
151. Boal, D.H., 1994, Computer simulation of a model network for the erythrocyte cytoskeleton, Biophys. J.